Coupling rare earth element analyses and high-resolution topography along fault scarps to investigate past earthquakes: A case study from the Southern Apennines (Italy)

Simone Bello[1,2,*], Maria Grazia Perna[1,*], Ada Consalvo[3], Francesco Brozzetti[1,2], Paolo Galli[4,5], Daniele Cirillo[1,2], Carlo Andrenacci[1,2], Anna Chiara Tangari[1], Andrea Carducci[1,2], Marco Menichetti[2,6], Giusy Lavecchia[1,2], Francesco Stoppa[1], and Gianluigi Rosatelli[1]

[1]Dipartimento di Scienze Psicologiche, della Salute e del Territorio (DiSPuTer), University G. d'Annunzio Chieti-Pescara, 66100 Chieti, Italy
[2]Centro inteRUniversitario per l'analisi Sismotettonica Tridimensionale (CRUST), 66100 Chieti, Italy
[3]Center for Advanced Studies and Technology (CAST), University G. d'Annunzio Chieti, 66100 Chieti, Italy
[4]Dipartimento della Protezione Civile, 00193 Rome, Italy
[5]Istituto di Geologia Ambientale e Geoingegneria (IGAG) del Consiglio Nazionale delle Ricerche (CNR), Monterotondo 00016 Rome, Italy
[6]Department of Pure and Applied Sciences, University of Urbino, 61029 Urbino, Italy

ABSTRACT

The systematic study of faults that have released strong earthquakes in the past is a challenge for seismic hazard assessment. In carbonate landscapes, the use of rare earth element (REE) concentrations on slickensides may aid the reconstruction of fault slip history. We applied this methodology to the Caggiano normal fault (Southern Apennines, Italy), cropping out southeast of the Irpinia 1980 CE earthquake fault (M_w 6.9), which was responsible for both the 1561 CE and partly the 1857 CE Basilicata earthquakes (M_w 6.7 and 7.1). We integrated the REE analysis approach with a high-resolution topographic analysis along 98 serial topographic profiles to measure vertical separations attributable to faulting since the Last Glacial Maximum (LGM). The asymmetric scarp height profiles suggest fault-lateral propagation and along-strike variations in the fault evolution. Our results indicate the occurrence of 7 to 11 earthquakes with variable slip between ~40 cm and ~70 cm within post-LGM times. We estimated the magnitudes of the respective earthquakes, between 5.5 and 7.0, and most commonly between 6.3 and 6.5. The results suggest a recurrence time between 1.6 k.y. and 2.3 k.y. and a slip rate ranging between 0.6 mm/yr and 0.9 mm/yr. This approach may be useful for application to carbonate fault planes in similar tectonic contexts worldwide.

■ INTRODUCTION

Italy is among the most seismically active areas of the entire Mediterranean basin, and it hosts extensional, compressional, and strike-slip earthquakes (e.g., de Nardis et al., 2022; Di Luccio et al., 2005; Herrmann et al., 2011; Pondrelli et

Simone Bello ⓘ https://orcid.org/0000-0002-1175-1083
*simone.bello@unich.it; mariagrazia.perna@unich.it

al., 2006; Scognamiglio et al., 2006). Major extensional earthquakes concentrate along the Apennine chain in the so-called extensional seismogenic province (sensu Lavecchia et al., 1994, 2021). This province extends with an average NW-SE direction along the axial zone of the Apennines (Galadini and Galli, 2000; Lavecchia, 1988) and continues with a N-S strike in northern Calabria (Andrenacci et al., 2023; Brozzetti et al., 2009, 2017a, 2017b; Cirillo et al., 2022b; Napolitano et al., 2021; Tortorici et al., 1995) and a NNE-SSW strike in southern Calabria (Cucci, 2022; Galli and Bosi, 2003; Neri et al., 2020). In this active geological environment, the faults often form rock scarps, facilitated by Bahamian-type Mesozoic–Cenozoic carbonate rocks. These well-preserved rock scarps may reach up to tens of meters in height and stretch along the edges of great intramontane Quaternary basins for hundreds to thousands of meters (Brozzetti, 2011; Brozzetti et al., 2019, 2020; Bucci et al., 2013; Civico et al., 2018; Galadini and Galli, 2000; Galli et al., 2006; Galli and Peronace, 2014; Gori et al., 2011; Mirabella et al., 2011; Roberts and Michetti, 2004; Schirripa Spagnolo et al., 2021; Sgambato et al., 2020; Villani et al., 2018; Villani and Pierdominici, 2010). In some cases, these structures run in the highest portions of the main ridges, sometimes even with trends oblique to the ridges, where they form narrow intramontane along-strike elongated basins, some hundreds of meters long and filled with late Quaternary clastic deposits. This is the case for the 25-km-long Caggiano fault system (Mt. San Giacomo and Timpa del Vento segments in Galli et al., 2006), which, according to Bello et al. (2022b), could be the northern segment of a much longer system (Caggiano-Montemurro fault). The Caggiano-Montemurro fault is an ~65-km-long, SSW-dipping trans-ridge fault crossing a portion of the Monti della Maddalena ridge (Fig. 1), connecting the Auletta and Val d'Agri basins and bordering the northernmost portion of the Vallo di Diano (Fig. 1). The Caggiano-Montemurro fault was recently hypothesized to be the main fault of the area, with a length capable of generating the 1857 CE (M_w 7.1) earthquake (Bello et al., 2022b). In turn, previous paleoseismological investigations across the Caggiano fault by Galli et al. (2006, 2008) accounted for several surface-faulting
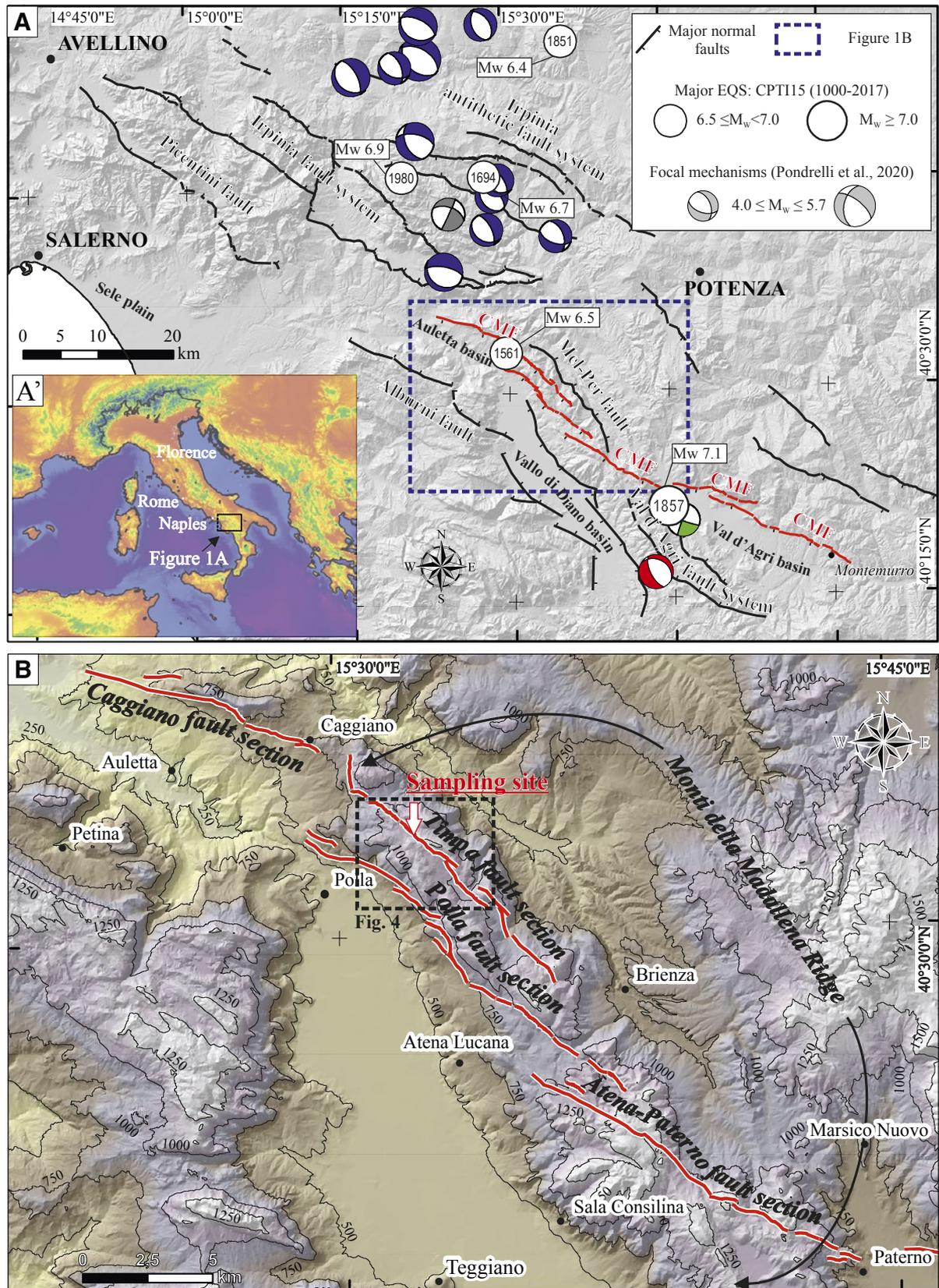
Figure 1. (A) Seismotectonic map of the Campania-Lucania extensional belt. Major normal faults are from literature (Bello et al., 2021a, 2022b; Brozzetti, 2011; Galli and Peronace, 2014). Major earthquakes (EQS) with $M_w \geq 6.5$ that occurred in the area from 1000 CE to 2020 CE are reported as white circles from the CPTI15 catalog (Rovida et al., 2020, 2022). Earthquake focal mechanisms (0–15 km; $4.3 \leq M_w \leq 6.8$; 1962–2002; blue—normal; green—strike-slip) are from Pondrelli et al. (2020). The red focal mechanism is from López-Comino et al. (2021). (A′) Location map of panel A. (B) Hillshaded relief map of the study area. Black dashed rectangle is the area of Figure 4A. Red lines are the northern segments of the Caggiano-Montemurro fault (CMF).

events in the past 6 k.y. The latest ones occurred in the last 2 k.y. B.P., probably during/after slope-debris deposition related to the Little Ice Age (ca. 1400–1800 A.D.). According to Castelli et al. (2008), both of the fault segments comprising the Caggiano fault were responsible for the two 1561 CE main shocks (31 July and 19 August 1561 CE; cumulative M_w = 6.7 in the Catalogo Parametrico dei Terremoti Italiani [CPTI15]), and, tentatively, also the northernmost shock of the devastating 1857 CE earthquake sequence (cumulative M_w = 7.0).

In recent years, many advances have been made to study coseismic deformation at the surface using high-resolution topography (e.g., Bello et al., 2021b; Bubeck et al., 2015; Cirillo, 2020; Johnson et al., 2014; Westoby et al., 2012; Wilkinson et al., 2015, 2016). In fact, high-resolution imagery and topography from light detection and ranging (LiDAR) and unmanned aerial vehicle (UAV) technologies provide excellent data sets for measuring fault scarps (e.g., Bello et al., 2022a; Scott et al., 2022; Stewart et al., 2018; Wilkinson et al., 2015; Wolfe et al., 2020). The high-precision measurements obtainable allow more in-depth studies, pushing forward the frontier of knowledge on old topics, like past earthquakes. Small UAVs can be equipped with onboard real-time kinematic global navigation satellite system (GNSS/RTK) antennas working with the post-processing kinematic (PPK) technique. The latter allows the acquisition of georeferenced photographs (centimeter-scale resolution) without placing ground-control points (Bolkas, 2019; Cirillo et al., 2022a; Cledat et al., 2020; Vichi et al., 2022; Zhang et al., 2019).

With the help of a MATLAB algorithm, a recently developed technique allows semi-automatic measurement of the vertical displacement along the active fault strike (Bello et al., 2021b; Scott et al., 2020). This code, which permits the measurement without losing control by the geoscientist, is valuable to constrain both the vertical displacement due to coseismic ruptures and the vertical displacement of long-term scarps. Although this approach is extremely useful because it provides an estimate of the scarp height potentially attributable to deformation since the Last Glacial Maximum (ca. 18 ka; post-LGM hereafter), it is not able to provide details of the number of earthquakes and the displacement likely associated with each of them.

A new approach that could allow researchers to quantitatively hypothesize the number of past earthquakes recorded by a fault scarp is to analyze, from a geochemical point of view, the concentration of certain chemical elements in the fault planes. In fact, carbonate fault planes react geochemically with the environment to which they are subjected, being enriched or depleted in certain chemical elements as a function of the exposure time. In particular, Benedetti et al. (2002, 2013), Palumbo et al. (2004), Schlagenhauf et al. (2011), and Pousse-Beltran et al. (2022) investigated the postglacial earthquake record by analyzing bedrock fault planes using ^{36}Cl cosmogenic dating. The methodology was applied on the Sparta fault (Greece) by Benedetti et al. (2002), on the Fucino basin fault (Italy) by Benedetti et al. (2013), on the Magnola fault (Italy) by Palumbo et al. (2004) and Schlagenhauf et al. (2011), and on the Mt. Vettore fault (Italy) by Pousse-Beltran et al. (2022). Recently, Iezzi et al. (2021) combined a geodetic survey with the ^{36}Cl methodology on active normal faults near Athens, Greece. Carcaillet et al. (2008) and Mouslopoulou et al. (2011) were among the first to analyze the content of rare earth elements (REEs) in limestone fault planes to constrain the number

of earthquakes released in post-LGM times by the Magnola and the Spili fault (Greece), respectively. Finally, the ^{36}Cl dating and REE analyses were combined by Tesson et al. (2016) on the Pizzalto fault, in central Italy.

Both approaches (i.e., topographic displacement and geochemical analyses) are based on the same two principles: (1) Since the Last Glacial Maximum (ca. 18 ka; Galli et al., 2006), the effects of surface faulting on rocky fault scarps are preserved due to the higher rates of faulting compared to the effects of erosion/sedimentation and (2) any earthquake of such magnitude as to allow the rupture to propagate at the surface will exhume a new portion of the fault plane, adding it to the cumulative fault scarp. For this last reason, the fault plane is ideally divided into ribbons of variable height, each of which would represent a seismic event. By sampling portions of rock parallel to the slip direction, a "log" of the slip increments can be recorded, and geochemical analyses can then be carried out on this record. Of course, fault planes can also be exhumed by non-tectonic (erosional and landslide) processes, and thus a geological and paleoseismological check must first filter out false active faults from real ones.

In this study, we concentrated on the northern section of the Caggiano-Montemurro fault. This highly segmented "trans-ridge fault" shows a well-defined en échelon geometric pattern at multiple viewing scales. Following the most widely adopted criteria in the literature (i.e., by identifying geometric and structural complexities such as gaps, overlaps, underlaps, and sudden strike variations), Bello et al. (2022b) constrained four orders of fault surface segmentation for the Caggiano-Montemurro fault. The section on which we concentrated, called Timpa del Vento, exposes fault planes that are suitable for our analyses because of their lithology, the quality of the outcrops, and the logistical ease of reaching them with instruments (Figs. 1–3). We combined the methodology of the displacement discontinuity approach (measuring displacements with high-resolution topography) to obtain information on ~5 km of fault length along with a detailed geochemical study at one site defining the variations in the content of trace elements (e.g., REEs + Y) on the fault plane.

The goal was to assess the number of earthquakes potentially released by the Timpa del Vento fault section, and likely by the Caggiano-Montemurro fault, which is considered to be a segmented or branched-at-depth normal fault (Bello et al., 2022b; Cello et al., 2003; Soliva et al., 2008). Finally, we used empirical relationships to estimate earthquakes magnitude from fault slip (Leonard, 2010; Thingbaijam et al., 2017; Wells and Coppersmith, 1994; Wesnousky, 2008).

■ TECTONIC SETTING AND SITE DESCRIPTION

The study area is located in the axial sector of the late Miocene–Pliocene Southern Apennines fold-and-thrust belt, which was dissected in the Quaternary by extensional structures (Lavecchia et al., 1994, 2021, 2022; Brozzetti, 2011, and references therein). We refer the interested reader to the broad available literature (e.g., Mostardini and Merlini, 1986; Nicolai and Gambini, 2007; Scrocca et al., 2007; Vezzani et al., 2010) for a complete and detailed description of the paleogeographic domains involved in the construction of the mountain chain.

Bello et al. | REEs and high-resolution topography to investigate past earthquakes

The extensional fault system offsets preexisting compressive structures of the fold-and-thrust belt beginning in the early Pleistocene (e.g., Barchi et al., 2007; Brozzetti, 2011; Casciello et al., 2006; Di Naccio et al., 2013; Papanikolaou and Roberts, 2007; Schiattarella, 1998), with low to moderate slip rates (Galli, 2020; Galli et al., 2006; Papanikolaou and Roberts, 2007; Sgambato et al., 2020) generating intramontane basins filled with Quaternary clastic and fluvio-lacustrine deposits (Amicucci et al., 2008; Brozzetti et al., 2017b; Brozzetti and Salvatore, 2005; Bucci et al., 2020; Di Giulio et al., 2016; Robustelli et al., 2014; Villani and Pierdominici, 2010; Villani et al., 2019). In the study area, these are the Auletta, the Vallo di Diano, and, marginally, the Val d'Agri (Fig. 1) basins, which show southwestward-thickening tilted beds in the Auletta basin (Amicucci et al., 2008; Brozzetti, 2011) and northeastward-thickening tilted beds in the Vallo di Diano and Val d'Agri basins (Giano et al., 2000; Zembo et al., 2009). For the whole area, current stress field data from tectonic structures show NNE-SSW extension, with an approximately N032E-trending near-horizontal s3 axis (Bello et al., 2021a, 2022b), slightly deviating from the approximately NE-SW s3 axis highlighted further south (e.g., Brozzetti et al., 2009; Cirillo et al., 2022b) or further north (e.g., Castaldo et al., 2018; Ferrarini et al., 2015; Lavecchia et al., 2017; Mariucci and Montone, 2016) along the Apennine chain.

The study area framed in Figure 2 is located along the Monti della Maddalena ridge (Fig. 1B), which is the structural continuity of the Mt. Marzano carbonate massif, the latter of which is bordered by the Irpinia fault system (Fig. 1A). This ridge is made of Triassic to Cretaceous marine carbonate and dolomitic rocks and Cretaceous–Paleogenic limestones, capped by Miocene siliciclastic deposits and by arenaceous flyschoid formations (Pescatore et al., 1970). The study sites are characterized by the presence of a portion of the Caggiano fault, which was recognized to be active by Galli et al. (2006). At the footwall of the fault, beyond the cataclastic layer, the rock type is characterized by shelf-marginal facies consisting of massive or poorly bedded bioclastic rudstones and framestones. The rock fault scarp can be followed along the narrow (200–400 m) Timpa del Vento and Campo di Venere basins, where it also affects active decametric-scale alluvial fans (Galli et al., 2006). The carbonate fault plane of our sampling site is located uphill of the southeastern tip of the Timpa del Vento basin, a few hundred meters from the beginning of a bedrock saddle dividing the two basins (Fig. 2). The sampling site is characterized by a tectonically exhumed fault plane portion (higher portion of ~370 cm) plus a lower part that was recently (between 2006 and 2016) bulldozed for the construction of a dirt road. This allowed us to reach the fault plane with vehicles and to carry the necessary sampling instrumentation close to the plane. In this site, Holocene deposits cut and are in contact with the fault, and, thanks to recent excavation, it is possible to correlate the modern soil covering the fault plane until recently with the REE concentrations. Close to the site described here, the topographic depression deepens abruptly and begins to widen to reach, within 500–600 m, its widest portion. According to some boreholes described in Galli et al. (2006), the infilling deposits of the basins are represented by a few meters of clays and sands along with alternating layers of slope debris and volcanic ashes. These deposits represent the last episode of

a marsh environment related to the damming of the basin controlled by the fault. Below these continental deposits, boreholes showed ~15 m of yellowish and blue-gray sandy clays, attributable to the marine Pliocene section by Lucchetti (1943) and covering the bedrock.

■ DATA AND METHODS

High-Resolution Topography

In April 2022, we acquired 2677 photographs along part of the Timpa del Vento fault using a DJI Mavic 2 Pro drone and a Phantom 4 Pro V2 drone that flew at ~50–100 m altitude above ground level (Fig. 2A, inset A'). For the best positioning of the photographs, we used an Emlid Reach RS2 GNSS/RTK L1, L2, L5 base station, positioned in two central portions of the study area, and an antenna rover (L1/L2 RTK/PPK) installed on board both drones. In total, we covered ~5 km along the fault strike of the Timpa del Vento segment with an average imaging width of ~500 m (Fig. 4A). The acquired photographs were reviewed, and then those that were low quality, blurred, or taken during takeoff and landing were eliminated. We processed the photographs to produce dense point clouds, orthomosaics, and digital elevation models (DEMs) with the Agisoft Metashape Pro image-based photogrammetric modeling software (version 1.8.4; e.g., Bello et al., 2021b; James and Robson, 2012; Johnson et al., 2014; Westoby et al., 2012). We aligned the 2619 selected photographs and produced the models with high-quality settings that were exported with the default recommended resolution. The obtained accuracy of the models was ~3 cm in the horizontal and vertical directions. We built hillshade maps in ArcMap (ESRI ArcMap© 10.8) with a resolution of ~3 cm/pixel. The DEM we produced ranged from ~1000 to ~1200 m altitude above sea level and covered an area of ~3.2 km^2.

Vertical Separation Measurement

We mapped the Timpa del Vento fault at a fixed scale of 1:500 in ArcMap©, using the DEMs and orthomosaics produced as base maps (Fig. 4A). The fault trace is observable at the border of the small (i.e., 1–3 km^2) intramontane Quaternary basins for the entire extent of the DEM (Figs. 3 and 4A). As mentioned, the fault pattern is highly segmented, and, even at the large scale (i.e., 1–3 km), it is articulated in small portions that border small intramontane basins (Figs. 2A and 2B). Based on the mapped traces and the DEMs produced, we used a MATLAB algorithm developed by Scott et al. (2020) for use by Bello et al. (2021b) and investigated the topography to measure the vertical separation (*VS*) along 98 topographic profiles. This approach allowed us to measure the *VS* defined as the vertical distance between the linear surface projections at the hanging wall and footwall of the fault measured at the fault trace position. For normal to oblique-normal faults (i.e., dip-slip or dip-slip with a slight strike-slip component), this assumption is considered appropriate because the lateral
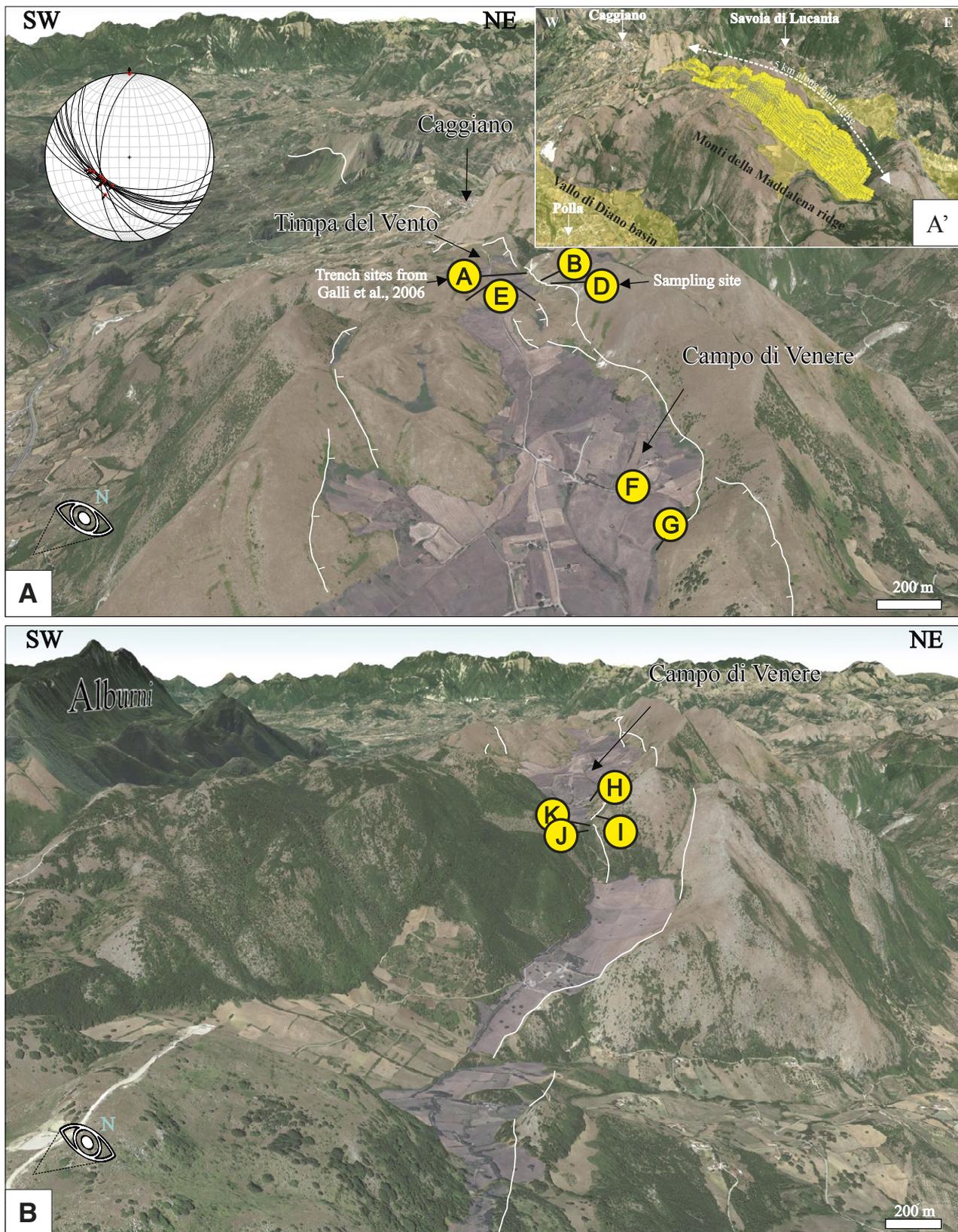
Figure 2. Bird's-eye view of the northern (A) and southern (B) portions of the study area along the Timpa del Vento and Campo di Venere basins. Yellow circles—locations of the photographic documentation in Figure 3. The sampling site of this paper and the trench site from Galli et al. (2006) are indicated in panel A and specifically correspond geographically with the locations of Figures 3D and 3A, respectively (indicated here with their respective yellow circles). The stereoplot in panel A represents the structural data (fault plane and slickenlines) acquired along the outcropping fault planes of the area. The shaded purple regions are the small intramontane Quaternary basins. (A') Location of the photographs taken to produce the high-resolution digital elevation model (DEM) and the orthomosaics.
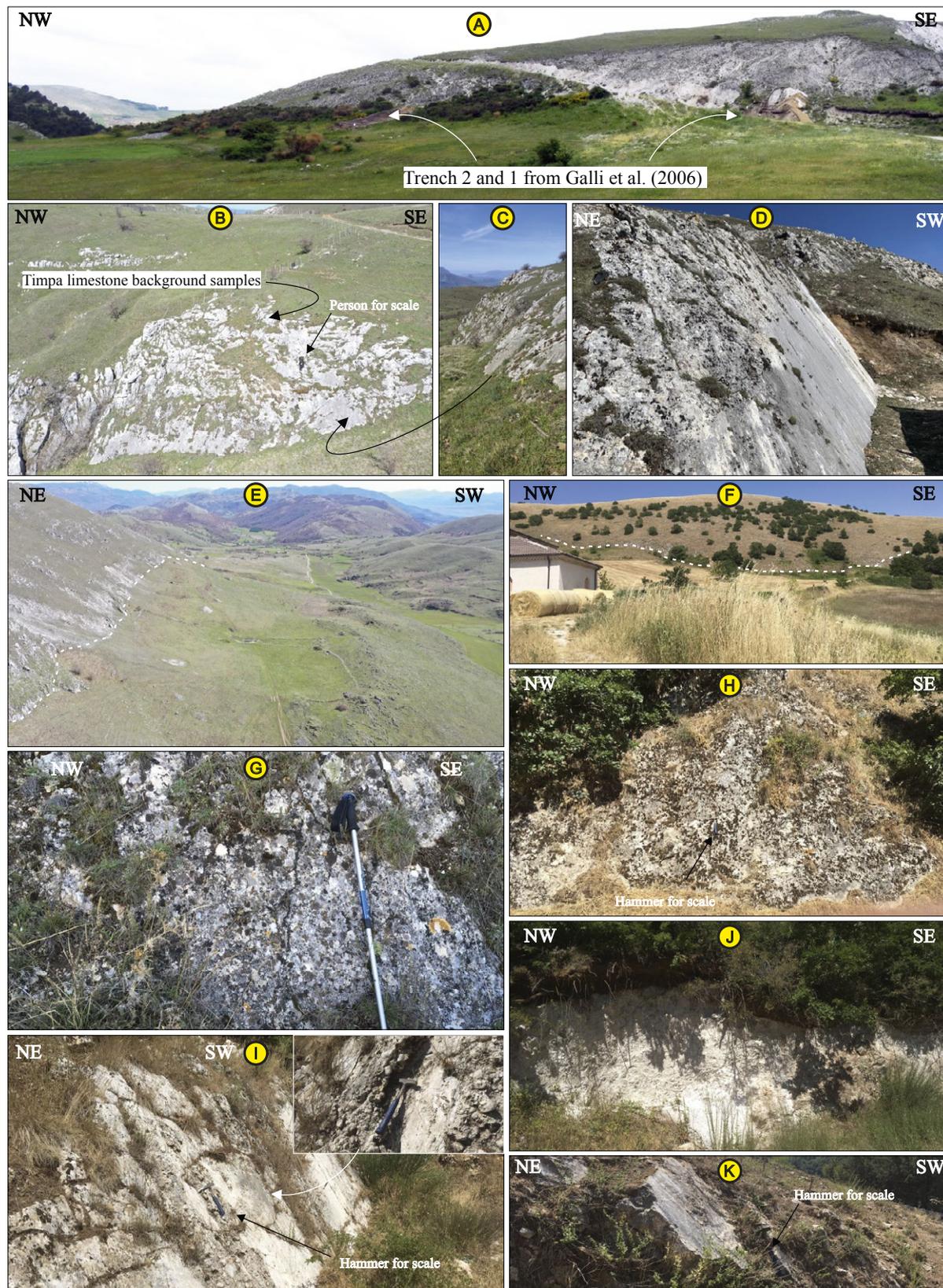
Figure 3. Photographic documentation of the fault planes of the Caggiano-Montemurro fault cropping out along the Timpa del Vento and Piano di Venere basins. The location of each photograph is indicated in Figure 2. (A) Location of trenches from Galli et al. (2006) along the Timpa fault section. (B) Drone photography of a fault plane along Timpa del Vento and location of the sampling site of the Timpa limestone background samples (LIM). (C) Detail of panel B. (D) Our sampling site with Holocene deposits cut by the fault and exposed due to anthropic exhumation of a portion of the fault plane. (E) Panoramic view of the Campo di Venere basin with the fault highlighted with the white dashed line. (F) Bedrock-Quaternary deposit contact along the Campo di Venere basin. (G–K) Striated fault planes along the southern portion of the Timpa fault (Campo di Venere basin).
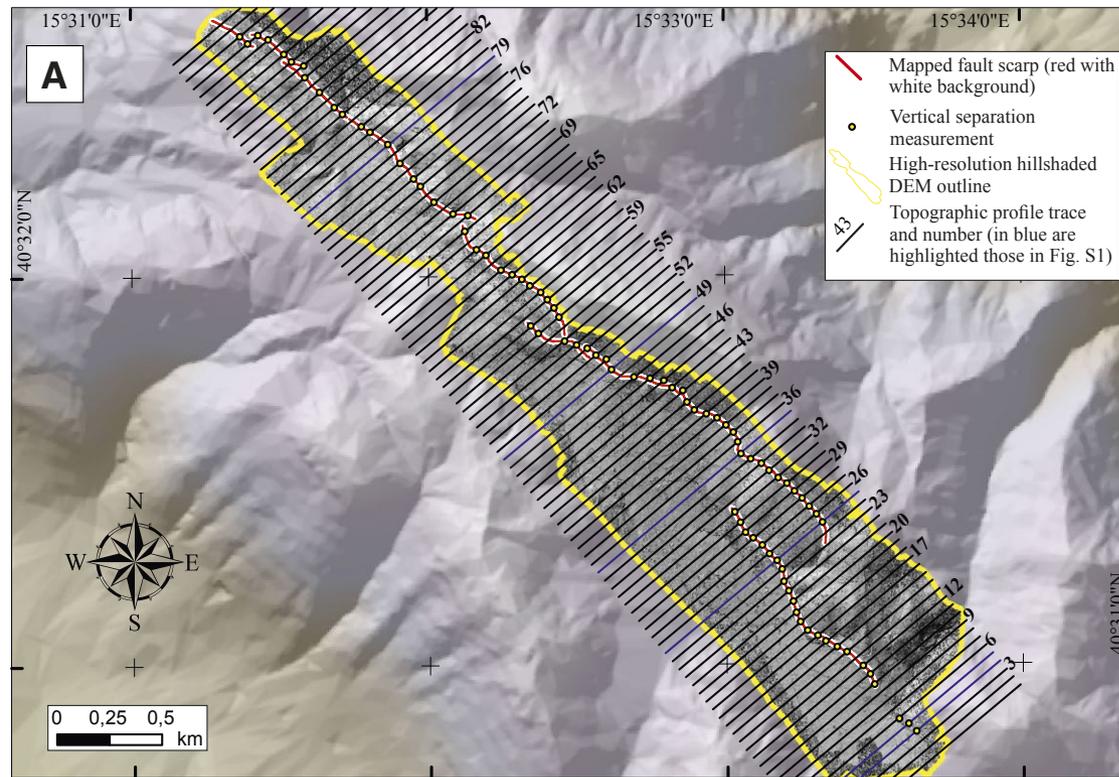
Figure 4. High-resolution topographic analysis of the study area. (A) Analyzed topographic profiles on the 3 cm/pixel digital elevation model (DEM) produced using the Agisoft Metashape Professional software. Blue topographic profiles traces are those of Figure S1 (see text footnote 1). (B) Example of a topographic profile on which a fault scarp with a vertical separation of ~3.8 m was measured. HW—hanging wall; FW—footwall; a.s.l.—above sea level.
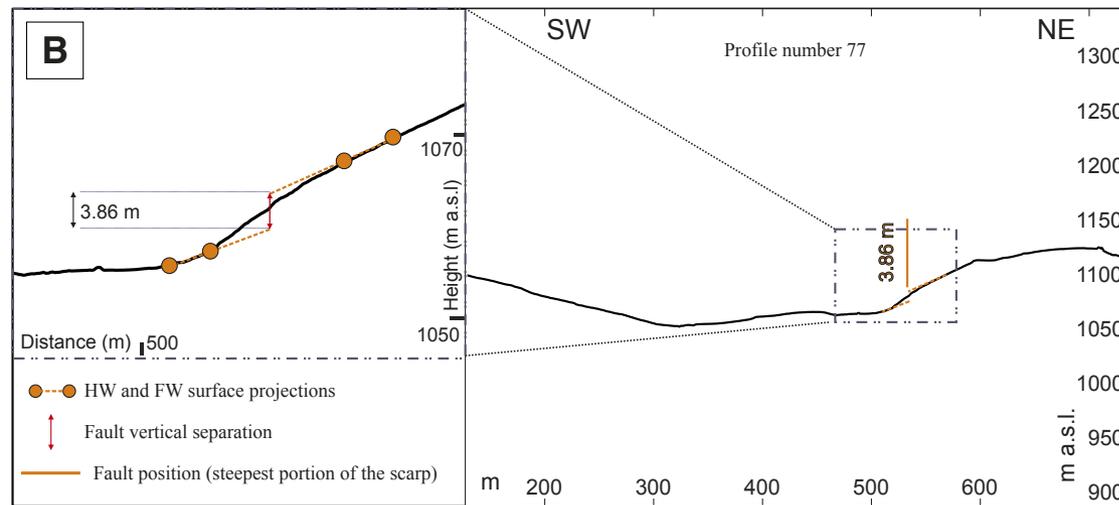
slip is thought to have minimal influence on the total displacement (Bello et al., 2021b; DuRoss et al., 2019; Scott et al., 2022). We reference the reader to Bello et al. (2021b) and to the user guide in Scott et al. (2020) for a detailed explanation of the steps for preparing the input files for the measurement process and a complete user guide of the MATLAB code.

We generated the topographic profiles, orientated perpendicular to the average fault strike (Fig. 4A), from the DEM with a 50 m spacing and a 2 m averaging window, which minimized the impact of the topography. To acquire the measurements, we manually marked two points on the hanging wall and two points on the footwall of the fault to provide the surface projection. The four points for the linear surface projections must be selected on bare ground, avoiding vegetation, which was easily identifiable on dense clouds, orthomosaics, DEMs, and topographic profiles (see details in Bello et al., 2021b; Scott et al., 2020). The position of the fault along the topographic profile was also manually picked by the operator and generally identified in the steepest part of the scarp face. The algorithm automatically measured the vertical separation. An example of one of the topographic profiles with the projection lines is shown in Figure 4B. The measurement was accompanied by a quality factor (measure quality ranking [MQR]), which characterizes the quality of the measurement based on parameters such as vegetation, the angle between the two linear surface projections (more or less regularized slope), and the ease of identification of the fault trace position. In addition, the measurements were accompanied by a statistical error, which was automatically calculated by the code as in the following equation by Bello et al. (2021b):

$$\Delta x = \sqrt{\left(m_{footwall} - m_{hanging\ wall}\right)^2 + \Delta Fx^2 + \Delta b_{hanging\ wall}^2 + \Delta b_{footwall}^2},$$

where $m_{footwall}$ and $m_{hanging\ wall}$ represent the best-fit slopes interpolated at the footwall and at the hanging-wall lines of the fault, while $b_{footwall}$ and $b_{hanging\ wall}$ are the topographic intercepts. ΔFx is 25% of the scarp height, representing the error in fault positioning (for details on the best-fit slopes calculations, see Bello et al., 2021b).

In total, we acquired 86 measurements on 76 transects considering the fault scarp near field, plus a further six measurements on six profiles considering the fault far field (i.e., the entire slope) and assuming a rough slope rectification during the strong LGM rhexistasy phases (ca. 24 ± 3 ka; Fig. S1[1]; Galli et al., 2012, 2017, 2022). Profiles and measurements will be described in the next sections.

Trace-Element Analyses

Sedimentary limestones are generally REE-poor (e.g., Rosatelli et al., 2023, and references therein; Stoppa et al., 2021), while the pedogenic environment

---

[1]Supplemental Material. Contains Figures S1–S3. Please visit **https://doi.org/10.1130/GEOS.S .23066144** to access the supplemental material, and contact editing@geosociety.org with any questions.

(soil) they are in contact with is generally enriched during its development. The contents of REEs and other high field strength elements (HFSEs) in soils are highly variable, depending on the properties of the parent material, the degree of weathering, the content of organic matter, biological activity, and the presence of clay minerals, Fe/Mn oxides, phosphates, and hydroxides (Cao et al., 2001; Kabata-Pendias, 2010; Tangari et al., 2018, 2021; Tyler, 2004). In the uppermost part of the soil, REE forms organic complexes (Pourret et al., 2007), preventing their leaching and transfer to the deeper part of the soil. Thus, REE + Y enriches the organic-richer soil portion (Carcaillet et al., 2008, and references therein). Primary (i.e., limestone) and secondary (i.e., cement) carbonates easily dissolve in the presence of any fluids acidified by dissolved CO_2. Fault planes developing in limestone produce breccias subject to dissolution by rain and circulating (vadose) waters. As explained in detail by Carcaillet et al. (2008), the dissolution of carbonate along an exposed fault plane produces REE + Y enrichment in the runoff waters. These waters reach the pedogenized colluvial wedge at the base of the fault scarp, where REE + Y forms organic complexes (Pourret et al., 2007) and/or is taken up by specific bacteria (Chen et al., 2000), enriching the topsoil and its fluids. These fluids produce reprecipitation of carbonates on the fault plane. Elements with similar ionic radius and valence similar to Ca^{2+} (e.g., Mg, Sr, P, Mn^{+2}; Carcaillet et al., 2008, and references therein) may enter the new carbonate crystal lattice. Other elements, including REE + Y, however, are not readily incorporated into the cement (Rosatelli et al., 2010), but they are fixed by bacterial, algae, and root activity along grain boundaries (Carcaillet et al., 2008). Therefore, the REE + Y concentration peaks during quiescent earthquake periods in the fault scarp portion in contact with topsoil. The estimated time for the REE + Y enrichment in a limestone fault scarp is 0.7 k.y. (Carcaillet et al., 2008). Once the enrichment is established, it remains constant regardless of the length of the time of the soil–fault scarp contact (see residence time in Carcaillet et al., 2008). Therefore, there is not a linear correlation between residence time (earthquake interval) and REE + Y concentration unless the earthquake interval is less than 0.7 k.y. In addition, the REE + Y enrichment processes are linked to organic complexation and soil activity, so variations in environmental parameters affecting both weathering processes and soil organic production would affect the rate of REE + Y buildup. The exchange process stops at the time when the fault plane is exposed due to exhumation (slope erosion processes or surface faulting). The conceptual model in Figure 5 shows the principle of a carbonate bedrock fault plane enriched with REEs by modern soil.

Sampling Strategy

The samples for the bulk chemical analyses were acquired from a carbonate fault plane outcropping along the Timpa del Vento fault (Figs. 3D, 6, and 7A). For sample extraction, we used a 900 W, 115 mm grinder on which we installed a 3-cm-diameter and 4-cm-long diamond coring cup powered by an electric-powered generator (Fig. 6). On the fault mirror, the kinematic indicators
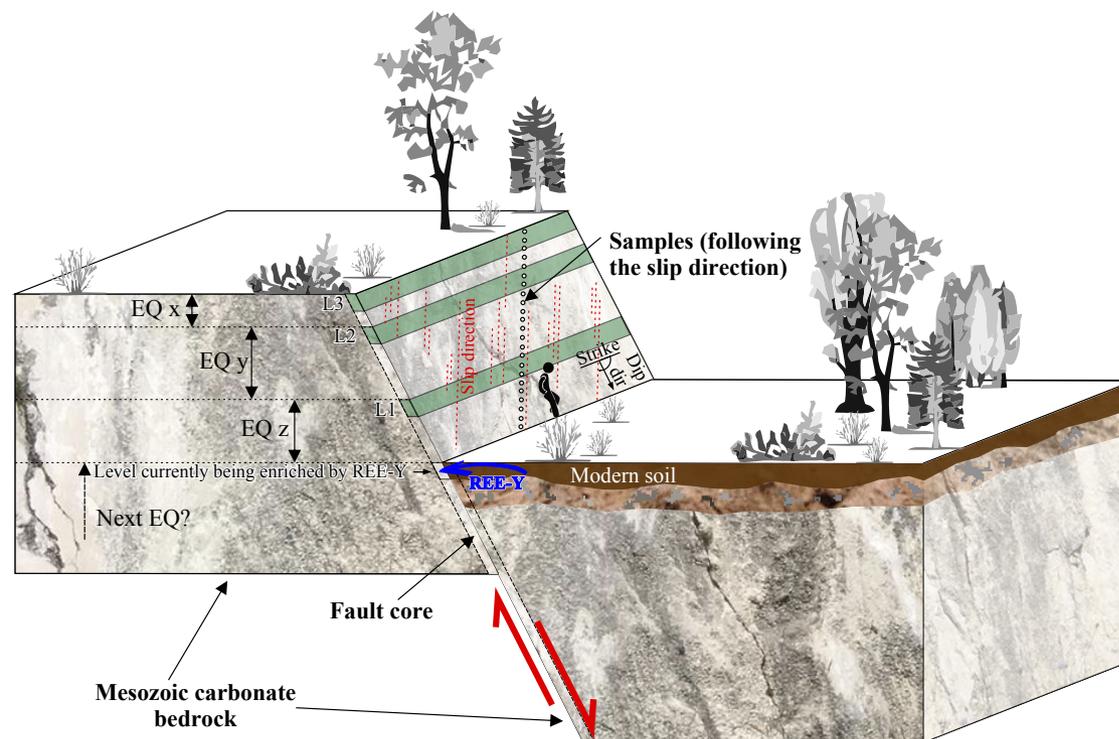
Figure 5. Conceptual three-dimensional model (not to scale) that explains the principle behind our study (adapted from Mouslopoulou et al., 2011). The soil, rich in rare earth elements + Y (REE-Y), enriches the carbonate of the fault plane with which it is in contact until the moment in which it is exhumed due to a seismic event of such magnitude as to be able to break the topographic surface. The mechanism is repeated with each earthquake causing surface faulting. The displacement associated with an earthquake (e.g., EQx in this figure) is given by the distance between the top of an enriched level (e.g., L3 in this figure) and the top of the next enriched level (e.g., L2 in this figure).

(i.e., slickenlines and calcite steps) show a sense of motion with a slight right-lateral component (rake = –116.3°, in Aki-Richard's format; see the stereoplot in Fig. 2A), which we considered as the correct direction line for the sampling. We laid a wire tied to two nails, positioned one on the head and the other at the base of the scarp, parallel to the slip direction (considering the slickenside). Starting from the highest part, we cored the fault plane every 10 cm along the wire, in the best-preserved points (e.g., without pervasive fractures in the plane and vegetation), acquiring 37 limestone cores (Fig. 7B). We continued coring the fault plane every 20 cm in the lower portion, which had been recently bulldozed, acquiring further two samples (Fig. 7B). To have an external control over the subsequent analyses (samples as background to be compared with samples from the fault plane), we sampled three additional cores (hereinafter referred to as Timpa limestone background [LIM]) from an outcrop belonging to the same geological formation (Lower Cretaceous–Liassic carbonate platform deposits belonging to the Monte Marzano–Monti della Maddalena unit; sensu Pescatore et al., 1999), cropping out at the footwall of the fault (location in Fig. 3B) and therefore not in contact with any soil or colluvium. After sampling, we classified each sample, giving it an identifier, taking a photograph of the extraction location, and describing its characteristics such as the presence of more or less developed lichens on the exposed surface. The next steps took place in the laboratory.

Chemical Pretreatment

The 39 limestone sample cores from the scarp and the three Timpa limestone background (LIM1, LIM2, LIM3) samples were prepared for inductively coupled plasma–mass spectrometry (ICP-MS) analysis. The first step was washing with 5 mL of 99.8% acetic acid to remove the dust from the drilling. We used a mini-drill to remove the surface patina affected by lichens and weathering. Then, the mini-drill was used to collect a 2 mm portion of carbonates from the external surface of the cores. Special care was taken to avoid as much as possible the limestone grains in the fault breccia and collect the carbonate cement among them. This powder was dried at 105 °C and weighed and then washed with 5 mL of ultrapure 130 vol% hydrogen peroxide for removal of organic matter, dried, and weighed again. The powder was dissolved with 5 mL of 2 N ultrapure hydrochloric acid at 80 °C, assuring the dissolution of calcite and dolomite. The dried solution was diluted with 5 mL of ultrapure

Bello et al. | REEs and high-resolution topography to investigate past earthquakes

Figure 6. Core drilling and sampling operations on the Timpa del Vento fault plane. GNSS—global navigation satellite system.

nitric acid at 65%. The method adopted here was similar to that of Carcaillet et al. (2008) and Mouslopoulou et al. (2011) but adapted to our sample suite.

ICP-MS Analysis

Each solution was subjected to analysis by ICP-MS, looking for trace-element concentrations. The instrument used was an Agilent 7900 ICP-MS (Agilent Technologies, Tokyo, Japan) in the laboratory of newborn screening, proteomics, and endocrinology of the Center for Advanced Studies and Technology (CAST), University of Chieti. Detailed operating conditions and instrumental parameters are given in Table 1. The fourth-generation Octopole Reaction System (ORS) was able to measure all elements in helium (He) mode, even though low-mass elements are normally measured in "no gas" mode due to the lack of interferences (Balcaen et al., 2015). The optimization of ICP-MS was carried out to obtain maximum signal intensities for ^{7}Li, ^{89}Y, ^{140}Ce, and ^{205}Tl using a 1 µg L^{-1} tuning solution containing Li, Y, Co, Ce, Mg, and Tl (Agilent Technologies, Palo Alto, California), while keeping the formation of

oxides ^{140}CeO$^+$/^{140}Ce$^+$ and doubly charged species Ce2$^+$/Ce$^+$ ratios below 1% and 3%, respectively. The sample introduction system was washed between different analyses with 2% HNO$_3$. Three multi-element mixtures at 10 µg mL^{-1} were used in acid solution:
- (A) Ag, Ba, Be, Cd, Co, Cr, Cu, Fe, Mn, Ni, Pb, Rb, Se, Sr, Tl, U, V, and Zn in 5% HNO$_3$;
- (B) Ce, Dy, Er, Eu, Ga, Gd, Ho, In, La, Lu, Nb, Nd, Pr, Sm, Th, Tb, Tm, Y, and Yb in 5% HNO$_3$; and
- (C) Hf, Nb, Sn, Ta, and Zr in 5% HNO$_3$.

These mixtures were employed to prepare daily diluted calibration solutions, and three calibration curves were prepared using these multi-element mixtures. An internal standard correction was performed by online addition of an internal standard solution of Rh (50 mg L^{-1}) in a T-piece. Ultrapure water (18 MΩ cm^{-1}) was obtained from a Milli-Q system (Millipore, Bedford, Massachusetts). Nitric acid (69% v/v) and an internal standard solution of Rh were bought from Merk (Darmstadt, Germany) and were ultrapure grade. The full data set was recorded with Agilent MassHunter Data Acquisition software (v. 4.2) and processed with the Agilent MassHunter Data Analysis software (v. 4.2).
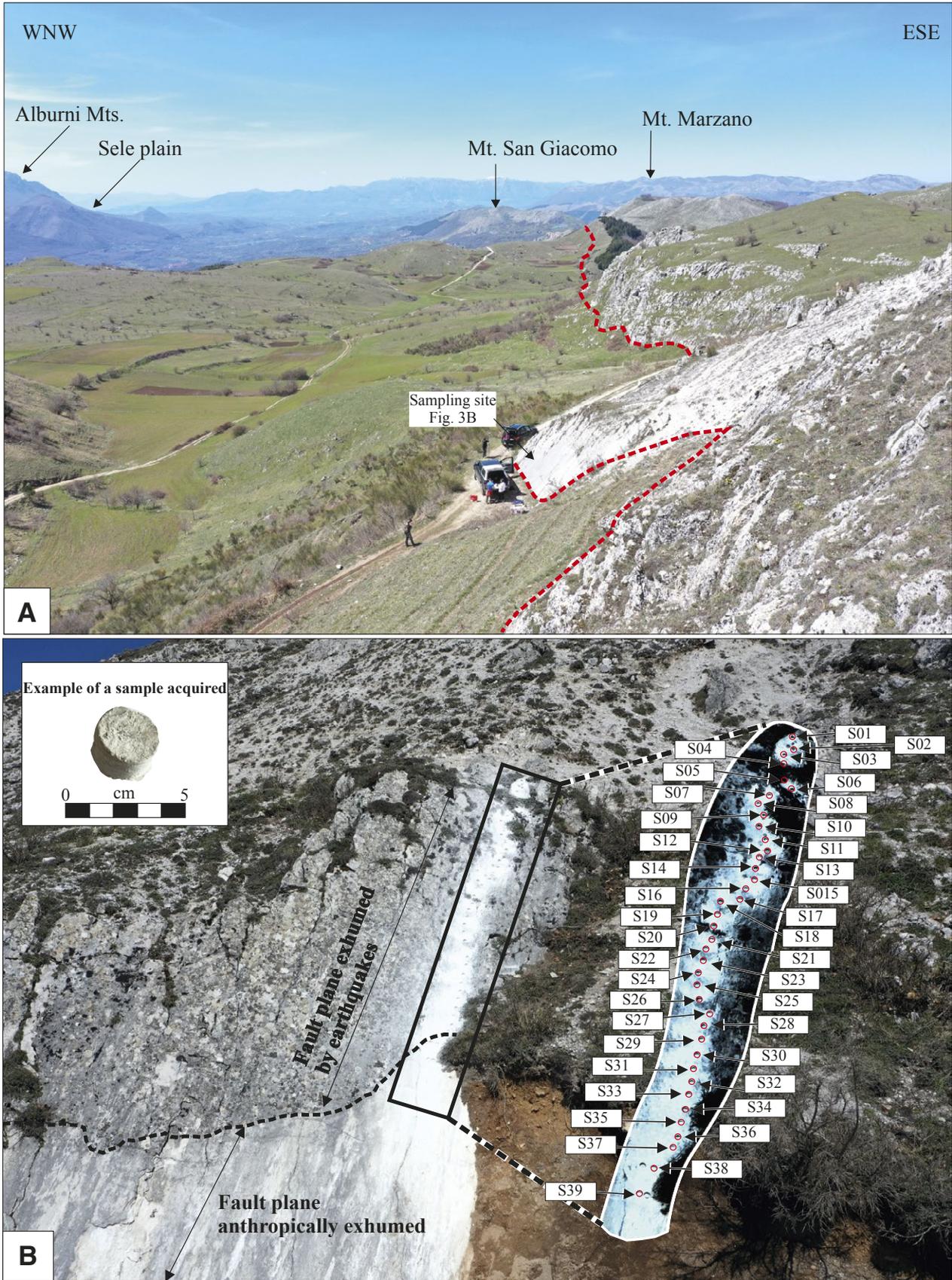
Figure 7. (A) Panoramic view of the Timpa del Vento basin and sampling site. (B) Sampling site at the carbonate fault plane of the Timpa del Vento basin. Note the tectonically exhumed upper portion of the fault plane and the recently anthropically exposed portion. On the fault plane, the cores were sampled as described in the main text.

TABLE 1. INDUCTIVELY COUPLED PLASMA–MASS SPECTROMETRY
(ICP-MS) INSTRUMENTATION AND OPERATING CONDITIONS

Instrument parameters	Agilent 7900 (Agilent Technologies, Tokyo, Japan)
Nebulizer	Nebulizer, MicroMist, U-series
Torch	Quartz glass torch
Spray chamber	Scott double-pass type at 2 °C
Sample cone	Nickel, 1.00 mm aperture
Skimmer cone	Nickel, 0.45 mm aperture
Sampling depth	10 mm
Nebulizer	1.05 L/min
Auxiliary gas	1.0 L/min
Plasma gas	15 L/min
RF power	1550 W
RF matching	1.80 W
Detection mode	Spectral
Integration time	0.3 s
Repetitions	3
Sample uptake rate	0.10 mL/min

Radiocarbon Dating

At our sampling site (Figs. 3D, 6, and 7B), the anthropic excavation aside the slickenside exhumed one brownish paleosol, truncated upward and mantled by a brownish pedogenized level, both developed on a volcanic layer. We sampled both levels (see Fig. S2) for radiocarbon dating to constrain the age by radiocarbon analyses. The two samples were named TDV18–01 (upper one) and TDV18–02 (lower one). The analyses were performed on bulk soil samples using the accelerator mass spectrometry (AMS) technique at the Beta Analytic (Miami, Florida) laboratories. Samples were physically pretreated to remove roots or macrofossils and acid washed to remove carbonates. The measured radiocarbon ages were calibrated using the software CALIB 8.2 (Stuiver et al., 2021); for further details and for standards and analytical protocols see details available at http://www.radiocarbon.com/.

■ RESULTS

Surface Expression of the Fault Scarp

The analysis of the topographic profiles through the MATLAB algorithm (see Methods section) allowed the measurement of the vertical displacement on 76 topographic profiles out of 98 (Figs. 4 and 8A). The 22 profiles on which we did not acquire measurements were affected by complexities including man-made structures, such as roads, irrigation canals, quarries, or small landslides, and overdeveloped vegetation. The topographic profiles were traced every 50 m, roughly perpendicular to the main fault. On the profiles, we acquired 86 measurements of *VS* (Table 2; Fig. 8B). To characterize the

long-term deformation and the variation of the fault scarps mapped in the study area, we plotted the *VS* data on a section parallel to the fault strike (Figs. 8B, 8C, and 8D). In Figure 8B, we plotted all the acquired measurements, while in Figures 8C and 8D, we considered the MQRs assigned during the measurement phase, and thereby we did not plot the quality = 4 values (i.e., low quality). We then used statistical errors (see Methods section) to add error bars to each measurement on the graph. Following Bello et al. (2022a), we computed envelope curves using the "envelope" function of the Signal Processing Toolbox in MATLAB (http://www.mathworks.com), which traces the envelopes of the peaks of the input signal, interpolating over local maxima separated by a given sampling interval, for which the units are the units of the data input. In Figure 8D, the sampling intervals are 2 and 30 m. We plotted the data both by differentiating the measurements based on the continuity of the mapped scarps (i.e., not cumulative in overlapping portions; Fig. 8C) and by cumulative values (Fig. 8D).

The displacement profile is characterized by a complex along-strike sinuosity with variable displacement, which overall follows a fairly regular trend. The displacement values (only those with MQR = 1–3) reach a maximum of ~400 cm and a minimum of around 70 cm, with mean and median values of ~210 cm. There are two major peak areas, a milder one located between 700 and 1800 m from the origin, and a more pronounced one located between 3300 and 3800 m from the origin. The latter area matches a portion of the fault where two en échelon strands overlap for ~500 m. Overall, the data show a two-peak profile (dark red dashed line in Fig. 8D) with two large slightly asymmetrical enveloping "bells" that grow rapidly moving from NW to SE and gradually decrease from the peak area southeastward. Considering the topographic profiles shown in Figure S1, i.e., considering the entire slope from the far field with respect to the fault location, we observed post-LGM vertical displacements ranging between ~9 and ~18 m, with average values of ~14 m.

REE-Y Concentration and Variations on the Fault Plane

In Table 3, we reported the ICP-MS analyses for the 39 samples picked from the slickenside and the 3 LIM representing the marine bedrock. As mentioned in the Sampling Strategy section above, LIM are samples acquired at the footwall of the fault plane on the same geological formation to be used as background. They had an average ΣREE + Y content of 2.56 (±0.56 standard deviation) ppm, with a La/Lu$_N$ ratio (normalized to C1 chondrite of Sun and McDonough, 1989) of 5.58 (±2.02) (Fig. 9). LIM showed a very slightly negative Ce anomaly, prominent positive Eu anomaly, and variable Y content (Fig. 10). The Y variability is typical of limestones and can be related to sedimentation of Mn crusts with phosphate layers in the basin (Auer et al., 2016). The small Ce negative anomalies and the enhanced Eu positive anomalies, which determine high Eu/Eu* ratios (= Eu/√[Sm + Gd]; 12.2 ± 3.3 on average; Table 3; Fig. 9), can be related to the oxidation state of the waters (Madhavaraju et al., 2016). The bedrock LIM samples had V/Cr ratios between 25.7 and 30.6 (Table 3), i.e., well above
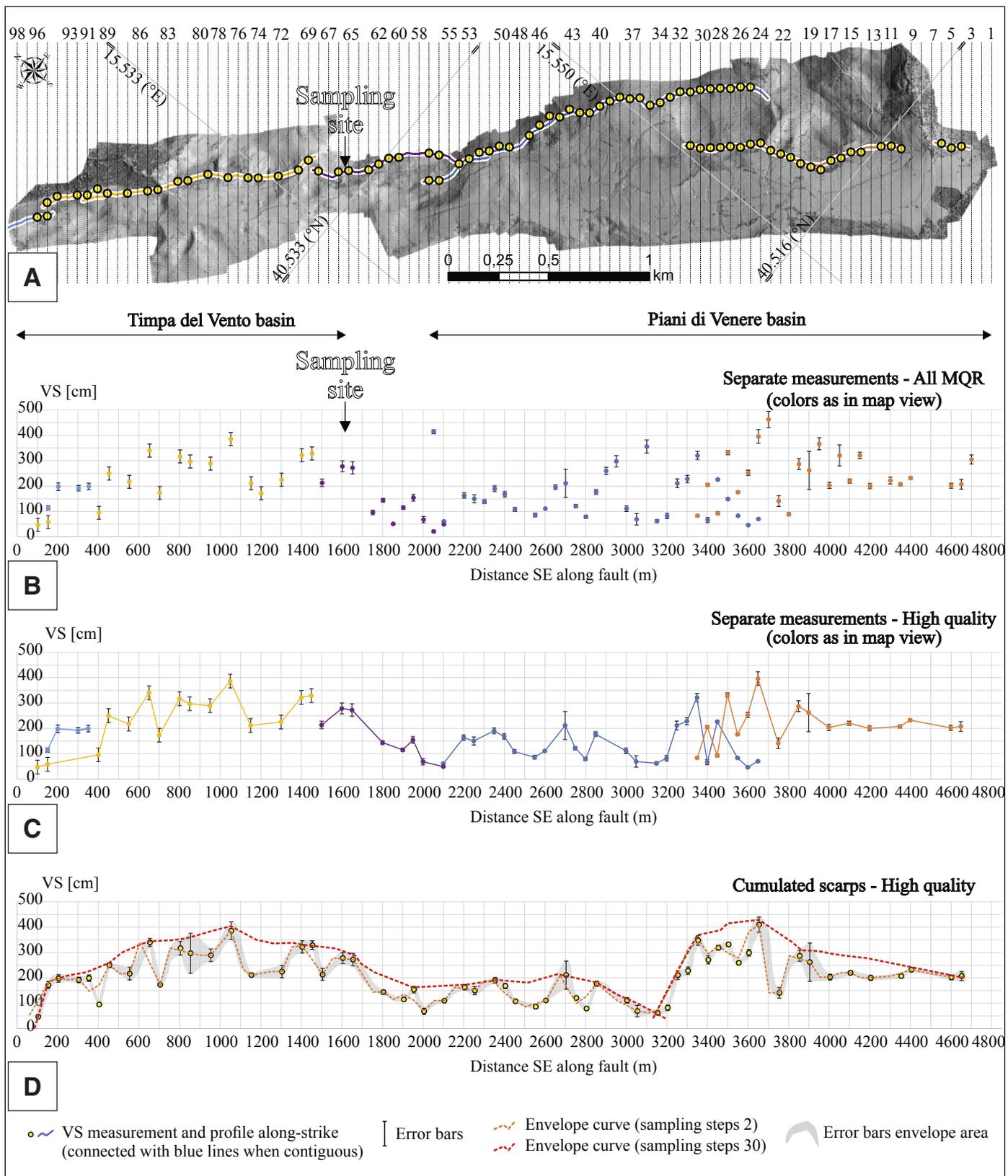
Figure 8. Along-strike distribution of vertical separation (*VS*) measurements acquired along the Timpa del Vento and Piano di Venere basins. (A) Topographic profiles used to measure the scarps on the high-resolution digital elevation model (DEM). (B) All measure quality ranking (MQR) measurements with colors referring to the color of the fault traces in A. (C) Same as panel A but without low-quality measurements. (D) Along-strike profile of the cumulated fault scarps. Error bars are the statistical error described in the Methods section.

TABLE 2. RESULTS OF THE TOPOGRAPHIC ANALYSIS MADE ON THE TOPOGRAPHIC PROFILES WITH THE MATLAB CODE

Ord. no.	Lat (°N)	Long (°E)	Elevation (m)	Topo. profile	Dip direction (°)	VS	MQR	Uncertainty
–	–	–	–	1	–	–	–	–
–	–	–	–	2	–	–	–	–
–	–	–	–	3	–	–	–	–
1	40.513774	15.560653	1023.3	4	218	305	3	35
2	40.514074	15.560202	1014.5	5	218	207	4	39
3	40.514552	15.560034	1010.7	6	218	202	4	20
–	–	–	–	7	–	–	–	–
–	–	–	–	8	–	–	–	–
–	–	–	–	9	–	–	–	–
4	40.515783	15.558281	1004.7	10	218	232	2	10
5	40.516212	15.558034	1011	11	218	207	3	13
6	40.516547	15.557639	1015.7	12	218	222	4	27
–	–	–	–	13	–	–	–	–
7	40.517078	15.556627	1016.6	14	218	200	3	20
8	40.517423	15.556249	1019.2	15	218	321	4	25
9	40.517603	15.555607	1013.4	16	218	220	3	17
10	40.517876	15.555114	1016.1	17	218	321	4	83
11	40.517959	15.554320	1006.6	18	218	203	3	24
12	40.518387	15.554072	1011.8	19	218	367	4	48
13	40.518831	15.553849	1014.5	20	218	262	3	151
14	40.519354	15.553752	1013.7	21	218	287	3	43
15	40.519802	15.553534	1015.4	22	218	89	4	13
16	40.520244	15.553309	1018.6	23	218	141	3	42
17	40.520808	15.553276	1025.1	24	218	463	4	64
18	40.521118	15.552840	1029.4	25	218	396	3	53
19	40.522757	15.555434	1089.4	25	233	70	2	7
20	40.521380	15.552330	1028.5	26	218	253	3	21
21	40.523107	15.555061	1094.3	26	233	46	3	6
22	40.521749	15.551988	1031.9	27	218	176	1	9
23	40.523407	15.554610	1100.8	27	233	83	3	6
24	40.522066	15.551564	1033.7	28	218	332	1	17
25	40.523768	15.554256	1107.9	28	233	149	4	10
26	40.522406	15.551178	1035.1	29	218	93	2	12
27	40.524096	15.553850	1118.4	29	233	226	3	8
28	40.522741	15.550782	1035.4	30	218	205	1	12
29	40.524412	15.553424	1127.2	30	233	66	3	20
30	40.523164	15.550525	1042.1	31	218	83	1	7
31	40.524696	15.552948	1132.8	31	233	321	3	32
32	40.525050	15.552583	1136.7	32	233	228	3	29
33	40.525240	15.551958	1119.6	33	233	211	1	35
34	40.525436	15.551343	1099.4	34	233	82	3	22
35	40.525703	15.550840	1090.2	35	233	62	3	12
36	40.526261	15.550798	1098.7	36	233	356	4	52
37	40.526589	15.550391	1092.09	37	233	69	3	45
38	40.526979	15.550084	1095.11	38	233	111	3	22
39	40.527211	15.549525	1094.70	39	233	298	4	44
40	40.527411	15.548916	1094.36	40	233	260	4	28
41	40.527565	15.548235	1099.40	41	233	177	2	19

(*continued*)

TABLE 2. RESULTS OF THE TOPOGRAPHIC ANALYSIS MADE ON THE TOPOGRAPHIC PROFILES WITH THE MATLAB CODE (*continued*)

Ord. no.	Lat (°N)	Long (°E)	Elevation (m)	Topo. profile	Dip direction (°)	VS	MQR	Uncertainty
42	40.527921	15.547873	1112.79	42	233	79	3	13
43	40.528363	15.547646	1128.24	43	233	121	2	13
44	40.528490	15.546922	1134.89	44	233	211	3	111
45	40.528866	15.546591	1146.10	45	233	196	4	18
46	40.528952	15.545802	1155.27	46	233	111	2	3
47	40.529003	15.544957	1155.02	47	233	86	1	15
–	–	–	–	48	–	–	–	–
48	40.529361	15.543673	1149.2	49	233	108	1	16
49	40.529736	15.543341	1149.2	50	233	168	3	21
50	40.529947	15.542750	1147.0	51	233	190	3	23
51	40.530253	15.542309	1155.7	52	233	139	4	16
52	40.530415	15.541639	1157.3	53	245	150	1	32
53	40.530618	15.541035	1164.1	54	245	163	1	21
–	–	–	–	55	–	–	–	–
54	40.530832	15.539523	1162.1	56	245	61	1	6
55	40.531558	15.540671	1194.5	56	230	49	1	5
56	40.531181	15.539150	1162.9	57	245	414	4	16
57	40.531962	15.540385	1192.7	57	230	21	4	9
58	40.532299	15.539993	1189.2	58	230	68	3	25
59	40.532644	15.539614	1189.4	59	230	154	1	26
60	40.532881	15.539063	1182.0	60	230	115	2	14
61	40.533201	15.538644	1185.1	61	230	51	4	6
62	40.533387	15.538012	1171.9	62	230	144	2	16
63	40.533564	15.537368	1167.4	63	230	96	4	18
–	–	–	–	64	–	–	–	–
64	40.534239	15.536585	1160.3	65	230	272	1	49
65	40.534548	15.536149	1147.3	66	230	278	2	43
–	–	–	–	67	–	–	–	–
66	40.535265	15.535432	1118.8	68	230	213	2	29
67	40.535921	15.535543	1124.6	69	226	329	1	34
68	40.535987	15.534723	1107.3	70	226	322	2	48
–	–	–	–	71	–	–	–	–
69	40.536509	15.533698	1112.2	72	226	225	2	49
–	–	–	–	73	–	–	–	–
70	40.537149	15.532860	1097.9	74	226	172	4	30
71	40.537498	15.532487	1089.6	75	226	211	1	12
–	–	–	–	76	–	–	–	–
72	40.538196	15.531741	1073	77	226	386	3	69
–	–	–	–	78	–	–	–	–
73	40.538985	15.531137	1068	79	226	289	1	49
–	–	–	–	80	–	–	–	–
74	40.539496	15.530096	1053.3	81	226	297	3	158
75	40.539827	15.529694	1049.9	82	226	317	3	54
–	–	–	–	83	–	–	–	–
76	40.540280	15.528560	1026.9	84	227	173	2	9
77	40.540587	15.528120	1037.6	85	227	340	2	31
–	–	–	–	86	–	–	–	–
78	40.541219	15.527269	1037.3	87	227	217	3	50

(*continued*)

TABLE 2. RESULTS OF THE TOPOGRAPHIC ANALYSIS MADE ON
THE TOPOGRAPHIC PROFILES WITH THE MATLAB CODE (*continued*)

Ord. no.	Lat (°N)	Long (°E)	Elevation (m)	Topo. profile	Dip direction (°)	VS	MQR	Uncertainty
–	–	–	–	88	–	–	–	–
79	40.541908	15.526508	1041.14	89	227	250	1	18
80	40.542387	15.526341	1045.49	90	233	95	2	9
81	40.542554	15.525679	1049.60	91	233	199	1	26
82	40.542901	15.525303	1065.76	92	233	192	1	22
–	–	–	–	93	–	–	–	–
83	40.543556	15.524488	1072.12	94	233	198	1	30
84	40.543340	15.523222	1024.58	95	236	58	3	11
85	40.543728	15.523834	1051.73	95	233	114	3	17
86	40.543653	15.522791	1021.52	96	236	47	2	9
–	–	–	–	97	–	–	–	–
–	–	–	–	98	–	–	–	–

Notes: Ord. no.—identifier for the measurement; Lat and Long—latitude and longitude in decimal degrees (dd.mmmmm) within the World Geodetic System (WGS) 1984 Universal Transverse Mercator (UTM) 33N coordinate system; Elevation—altitude expressed in meters above sea level (a.s.l.) extracted from the digital elevation model produced for this work; Topo. profile—topographic profile number (see Figs. 4 and 7) along which the measurement was acquired; Dip direction—direction of the trace dip with respect to north, expressed in degrees; *VS*—vertical separation measurement expressed in centimeters; MQR—measure quality ranking, given as a number between 1 and 4 indicating the quality parameter assigned to each measurement; Uncertainty—uncertainty of the *VS* measurement, expressed in centimeters. Empty rows are topographic profiles along which no measurements were acquired.

the value of 4.3, which is the upper limit of suboxic conditions. Thus, the V/Cr ratio of LIM indicates very reducing conditions in the limestone formation environment. The poorly oxygenated waters favored the reduction of Eu^{3+} to Eu^{2+}. Eu^{2+} is more compatible than REE^{3+} and so more prone to enter into the forming carbonate lattice.

Carbonates sampled on the fault plane (from S1 to S37 in Fig. 7; Table 3) above the present soil had very variable REE + Y contents with an average of 14.51 (±9.15) ppm (Fig. 10) and very variable La/Lu_N values with an average of 17.87 (±13.55) ppm (Fig 9). However, the ratio of light to heavy REEs (LREE/HREE) in the fault carbonate cements was higher than that in the Timpa limestone. An Eu anomaly was present in many but not in all of the fault carbonate samples. Where it was present, it was less pronounced than in the bedrock limestones, and the Eu/Eu* ratio was 1.61 (±1.2) on average (Fig. 9). Carbonate samples on the fault plane covered by the active soil (S38 to S39; Fig. 7; Table 3) were characterized by high REE + Y contents with an average of 23.43 (±6.44) ppm (Fig. 10), high La/Lu_N values between 8.47 and 11.61 (Fig. 9), and a low Eu/Eu* ratio with an average of 2.66 (±0.72) (Fig. 9). The data indicate that the soil at the contact with the fault plane scavenges REE + Y from the limestone breccia and deposits carbonate cements retaining some of the LIM characteristics, such as a negative Eu anomaly. However, the more

oxygenated soil environment produces oxidation of Eu^{2+} into Eu^{3+}, which can be incorporated into the newly formed cements with the same compatibility as the other REE^{3+} elements, reducing the Eu/Eu* ratio in those cements (Fig. 9). In the carbonate cements, the higher fractionation between LREEs and HREEs due to epigenetic crystallization is also evident (Fig. 9).

Figure 11 shows the variability of REE-Y concentration as a function of fault scarp height (cm). The vertical axis represents $\Delta i/\Delta m$, where Δi is the difference in concentration between each element and the average concentration of that element along the entire scarp ($Ci – Cm$), and $\Delta m = \Sigma|\Delta i|/N$, with N = number of measurements (39) (e.g., Carcaillet et al., 2008; Mouslopoulou et al., 2011). The interpretation and discussion of the possible earthquakes highlighted by the REE-Y variations shown in Figure 11 are given in the next section.

We show in Figure S3 the detrended distribution (i.e., the difference between each abundance distribution and its trend) of REE-Y contents for each element, performed using MATLAB functions. REEs do not show homogeneous behavior in terms of LREE/HREE. Using this representation, we highlight the fractionation of REEs in each sample compared to the general trend of each element along the fault scarp.

■ DISCUSSION AND CONCLUSIONS

Constraints on Fault Geometry and Characteristics

We investigated the northernmost portion of the Caggiano-Montemurro fault, a highly segmented active fault believed to be responsible, or partially responsible, for the 1857 CE (M_w 7.1) and 1561 CE (M_w 6.7) earthquakes (Bello et al., 2022b; Galli, 2020; Galli et al., 2006, 2008; Spina et al., 2008). Three trenches opened by Galli et al. (2006) (location in Figs. 2A and 3A) account for multiple surface-faulting events during the past 6.5 ka (cal. yr B.P.) and show that the latest of these events occurred in the past 2 ka (cal. yr B.P.), possibly during/after the deposition of the slope debris of the Little Ice Age (ca. 1400–1800 CE). The paleosol levels that we sampled for radiocarbon dating (see "Radiocarbon Dating" section) at the side of the fault plane shown in Figures 3D, 6, and 7B provided a calibrated age of ca. 23.7 ka (lower level, sample TDV18–02, 0.9 m below ground surface) and ca. 11.0 ka (upper level, sample TDV18–01, 0.7 m below ground surface) (Table 4). Considering these ages, the lower brownish paleosol was truncated upward by slope erosion at the onset of the LGM, whereas the upper brown level might have formed at the expense of the Neapolitan Yellow Tuff tephra, dated at 14.5 ± 0.4 ka by Galli et al. (2017).

The preservation of the rock-fault scarp mapped in continuity with an en échelon geometry and overlapping portions of the 5 km section investigated with high-resolution topography (Fig. 4) allowed us to reconstruct the deformation profile of the fault over the area. On average, the scarp height profiles in the study area are best fitted by an asymmetric triangular shape (i.e., major peaks shifted from the center of the profile; for detailed description, see Manighetti

TABLE 3. RARE EARTH ELEMENT + Y (REE-Y) CONCENTRATIONS MEASURED BY INDUCTIVELY COUPLED PLASMA–MASS SPECTROMETRY (ICP-MS)
FOR THE 39 LIMESTONE SAMPLE CORES FROM THE SCARP AND FOR THE THREE TIMPA LIMESTONE BACKGROUND SAMPLES

Sample no.	Scarp height (cm)	Y	La	Ce	Pr	Nd	Sm	Eu	Gd	Tb	Dy	Ho	Er	Tm	Yb	Lu	Σ REE	Σ LREE	Σ HREE	LREE/ HREE
S1	360	1.03	1.28	2.38	0.23	0.86	0.17	0.07	0.19	0.03	0.14	0.03	0.09	0.01	0.07	0.01	6.58	4.92	0.63	7.82
S2	350	0.98	0.90	1.00	0.13	0.47	0.09	0.04	0.11	0.02	0.09	0.02	0.06	0.01	0.06	0.01	3.95	2.58	0.40	6.41
S3	340	1.25	6.51	8.22	0.58	1.80	0.29	0.35	0.33	0.04	0.19	0.04	0.12	0.02	0.10	0.02	19.83	17.40	1.19	14.64
S4	330	2.33	2.64	4.31	0.47	1.77	0.35	0.10	0.39	0.05	0.30	0.06	0.19	0.03	0.16	0.03	13.19	9.53	1.32	7.21
S5	320	1.70	2.25	2.67	0.42	1.59	0.30	0.08	0.31	0.04	0.23	0.05	0.14	0.02	0.12	0.02	9.93	7.23	1.01	7.19
S6	310	2.37	2.84	4.60	0.53	1.98	0.38	0.10	0.41	0.06	0.30	0.06	0.19	0.03	0.16	0.03	14.03	10.32	1.34	7.69
S7	300	1.84	4.05	3.16	0.36	1.41	0.29	0.09	0.31	0.04	0.24	0.05	0.15	0.02	0.13	0.02	12.15	9.26	1.05	8.84
S8	290	3.67	4.82	8.39	0.94	3.67	0.75	0.20	0.78	0.10	0.54	0.11	0.32	0.04	0.24	0.04	24.60	18.57	2.36	7.87
S9	280	1.87	1.98	3.13	0.40	1.52	0.30	0.09	0.33	0.05	0.24	0.05	0.15	0.02	0.13	0.02	10.27	7.33	1.07	6.82
S10	270	2.77	15.75	20.19	1.69	5.22	0.79	0.42	0.91	0.10	0.48	0.09	0.27	0.03	0.21	0.03	48.96	43.64	2.55	17.13
S11	260	0.11	0.44	0.39	0.04	0.11	0.02	0.02	0.02	0.00	0.01	0.00	0.01	0.00	0.01	0.00	1.18	0.99	0.08	13.03
S12	250	0.18	0.55	0.56	0.05	0.19	0.03	0.03	0.04	0.01	0.03	0.01	0.01	0.00	0.01	0.00	1.70	1.39	0.13	10.34
S13	240	0.12	0.43	0.37	0.03	0.11	0.02	0.03	0.03	0.00	0.02	0.00	0.01	0.00	0.01	0.00	1.17	0.95	0.10	9.90
S14	230	2.26	5.10	8.51	0.75	2.65	0.48	0.16	0.53	0.07	0.35	0.07	0.22	0.03	0.17	0.03	21.37	17.49	1.62	10.78
S15	220	1.69	3.21	4.93	0.43	1.59	0.30	0.11	0.36	0.04	0.24	0.05	0.15	0.02	0.13	0.02	13.26	10.45	1.12	9.34
S16	210	2.28	3.79	6.95	0.69	2.56	0.50	0.15	0.55	0.07	0.36	0.07	0.22	0.03	0.18	0.03	18.41	14.48	1.66	8.75
S17	200	1.33	2.02	3.13	0.34	1.26	0.24	0.11	0.27	0.04	0.19	0.04	0.12	0.02	0.10	0.02	9.23	7.00	0.91	7.74
S18	190	1.25	1.65	2.45	0.30	1.11	0.22	0.09	0.25	0.03	0.18	0.04	0.12	0.02	0.09	0.02	7.80	5.73	0.82	6.98
S19	180	1.31	2.34	3.85	0.43	1.61	0.31	0.11	0.35	0.05	0.23	0.05	0.13	0.02	0.10	0.02	10.90	8.54	1.05	8.18
S20	170	1.58	12.06	10.97	0.90	2.53	0.35	0.86	0.47	0.05	0.22	0.05	0.15	0.02	0.12	0.02	30.32	26.80	1.94	13.84
S21	160	1.75	3.72	4.74	0.38	1.31	0.23	0.29	0.32	0.04	0.22	0.05	0.15	0.02	0.13	0.02	13.37	10.39	1.24	8.38
S22	150	1.56	3.51	4.62	0.48	1.66	0.30	0.14	0.36	0.05	0.25	0.05	0.16	0.02	0.14	0.02	13.31	10.57	1.19	8.92
S23	140	1.29	3.98	5.96	0.45	1.37	0.22	0.37	0.29	0.03	0.18	0.04	0.13	0.02	0.11	0.02	14.45	11.98	1.18	10.13
S24	130	1.47	2.69	3.80	0.34	1.18	0.22	0.18	0.28	0.04	0.20	0.05	0.15	0.02	0.13	0.02	10.77	8.23	1.07	7.70
S25	120	1.41	1.59	2.01	0.27	1.02	0.20	0.10	0.26	0.04	0.20	0.05	0.14	0.02	0.12	0.02	7.44	5.09	0.95	5.33
S26	110	2.40	4.05	6.81	0.81	3.15	0.65	0.21	0.75	0.10	0.50	0.11	0.32	0.04	0.27	0.04	20.20	15.46	2.34	6.60
S27	100	1.43	1.91	2.65	0.33	1.26	0.25	0.15	0.30	0.04	0.23	0.05	0.17	0.02	0.14	0.02	8.96	6.40	1.13	5.67
S28	90	1.87	3.06	4.60	0.52	1.97	0.38	0.25	0.49	0.06	0.34	0.08	0.24	0.03	0.21	0.03	14.14	10.55	1.73	6.10
S29	80	1.02	1.30	1.83	0.23	0.90	0.17	0.13	0.24	0.03	0.18	0.04	0.13	0.02	0.12	0.02	6.34	4.42	0.90	4.92
S30	70	1.92	3.46	5.00	0.63	2.40	0.47	0.19	0.61	0.08	0.42	0.09	0.28	0.04	0.23	0.04	15.86	11.95	1.98	6.03
S31	60	1.32	2.46	3.06	0.38	1.52	0.29	0.19	0.41	0.05	0.28	0.06	0.19	0.03	0.17	0.03	10.44	7.70	1.41	5.45
S32	50	1.71	2.72	3.38	0.42	1.65	0.32	0.19	0.46	0.06	0.34	0.08	0.24	0.03	0.23	0.04	11.85	8.48	1.66	5.11
S33	40	2.65	4.72	6.58	1.00	4.05	0.79	0.37	1.10	0.14	0.72	0.15	0.47	0.06	0.40	0.06	23.24	17.13	3.46	4.95
S34	30	2.84	5.22	3.33	0.95	3.88	0.70	0.37	1.02	0.13	0.70	0.15	0.48	0.06	0.40	0.06	20.30	14.07	3.38	4.16
S35	20	1.75	3.61	5.82	0.72	2.85	0.54	0.30	0.80	0.10	0.48	0.10	0.32	0.04	0.27	0.04	17.74	13.54	2.45	5.54
S36	10	2.32	4.87	6.95	0.90	3.62	0.67	0.44	1.12	0.13	0.65	0.14	1.03	0.06	0.40	0.06	23.34	17.01	4.02	4.23
S37	0	3.23	6.27	5.30	1.19	4.87	0.95	0.44	1.41	0.18	0.90	0.19	0.61	0.08	0.53	0.08	26.24	18.58	4.43	4.19
S38	-20	3.03	8.57	6.27	1.48	5.72	0.97	0.53	1.73	0.19	0.88	0.19	0.62	0.07	0.52	0.08	30.86	23.02	4.81	4.79
S39	-40	2.33	5.12	3.95	0.80	3.21	0.60	0.62	1.13	0.12	0.59	0.13	0.41	0.05	0.36	0.07	19.47	13.67	3.47	3.94
LIM1	Background concentration	0.36	0.32	0.39	0.04	0.36	0.05	0.36	0.04	0.02	0.06	0.01	0.03	0.00	0.03	0.00	2.08	1.17	0.55	2.11
LIM2		0.81	0.51	0.27	0.06	0.47	0.06	0.63	0.07	0.04	0.09	0.02	0.09	0.01	0.05	0.01	3.19	1.37	1.01	1.36
LIM3		0.27	0.29	0.23	0.05	0.40	0.07	0.79	0.07	0.04	0.06	0.01	0.07	0.01	0.05	0.01	2.41	1.04	1.11	0.93

Notes: ΣREE—sum of all REEs, from La to Lu; ΣLREE—sum of all light rare earth elements (LREEs), from La to Sm; ΣHREE—sum of all heavy rare earth elements (HREEs), from Eu to Lu; LREE/HREE—index of the degree of fractionation. All element measurements are in ppm.
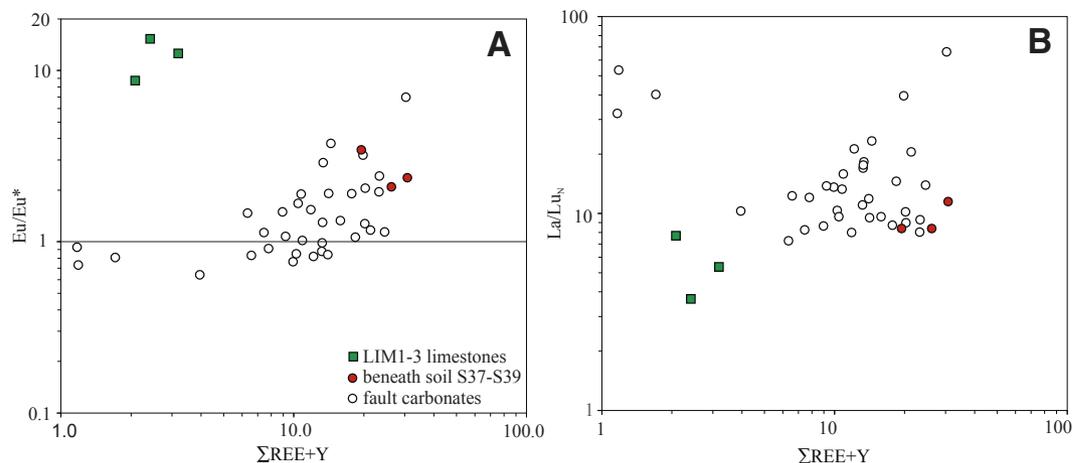
Bello et al. | REEs and high-resolution topography to investigate past earthquakes

Figure 9. (A) Total rare earth elements + Y (ΣREE + Y) compared to Eu/Eu* ratios of the samples analyzed. Note the highest Eu/Eu* ratio of the Timpa limestones (background). (B) Relation between ΣREE + Y and La/Lu$_N$ ratio. The cement precipitation increases the fractionation between light REEs (LREEs) and heavy REEs (HREEs) with respect to bedrock limestones.
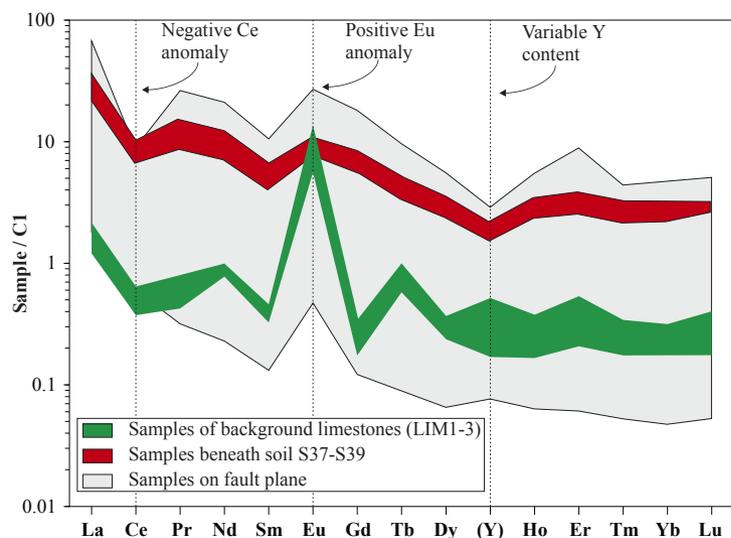

Figure 10. Pattern of rare earth elements + Y (REE + Y) for the Timpa limestone bedrock and fault carbonates normalized to chondrite C1. Figure highlights a positive Eu anomaly in limestone bedrock samples (LIM 1–3) (which is less pronounced in fault carbonates), and a very slightly negative Ce anomaly, both related to anoxic environment conditions during their formation. The Y variability can be related to sedimentation of Mn crusts with phosphate layers in the basin (see main text for details). The content of REE + Y in the fault carbonate samples (gray area in this figure) above the present soil is variable and averages 14.51 (±9.15) ppm (see Table 3). Fault carbonate samples on the fault plane covered by active soil are characterized by high REE + Y contents, which average 23.43 (±6.44) ppm.

et al., 2009), suggesting fault-lateral propagation and along-strike variations in the fault evolution (sensu Manighetti et al., 2009). Considering that the structure has recently been mapped for several tens of kilometers (Bello et al., 2022b), further research could be done to investigate the evolution of the structure with the method of high-resolution topography for scarp analysis. Indeed, the same measurement carried out on other exposed portions of the fault would allow the along-strike evolution to be reconstructed as completely as possible. This would allow hypotheses to be formulated about the average propagation direction of long-term ruptures as a whole, that is, those that most frequently characterize the earthquakes' entire structure. The propagation direction of earthquakes in this area, or at least those that have been associated with the Caggiano-Montemurro fault (i.e., 1561 CE and 1857 CE), is still a matter of discussion (Bello et al., 2022b). In the studied portion, the trend most frequently characterizing the earthquakes is that of propagation from north to south, as suggested by the two asymmetrical envelope lines reconstructed from our *VS* data. In general, this characteristic of slip profiles is considered as self-similar, indicating areas of maximum and minimum asperity, and a function of fault maturity (Manighetti et al., 2007, 2009). However, we are aware that since the portion of the fault investigated in this work was only 5 km long, our observations could represent a local trend and could fall into a larger-scale trend in a different way. In addition, as also suggested by Bello et al. (2022b), the remarkable segmentation of this fault, and its deviation from the general trends in the bordering large basins aligned instead in "transridge" alignment and generating small, suspended basins within the ridges, could be an index of lower maturity with respect to most of the known faults in the Apennines (e.g., Galli and Peronace, 2014). For all these reasons, subsequent studies are required.
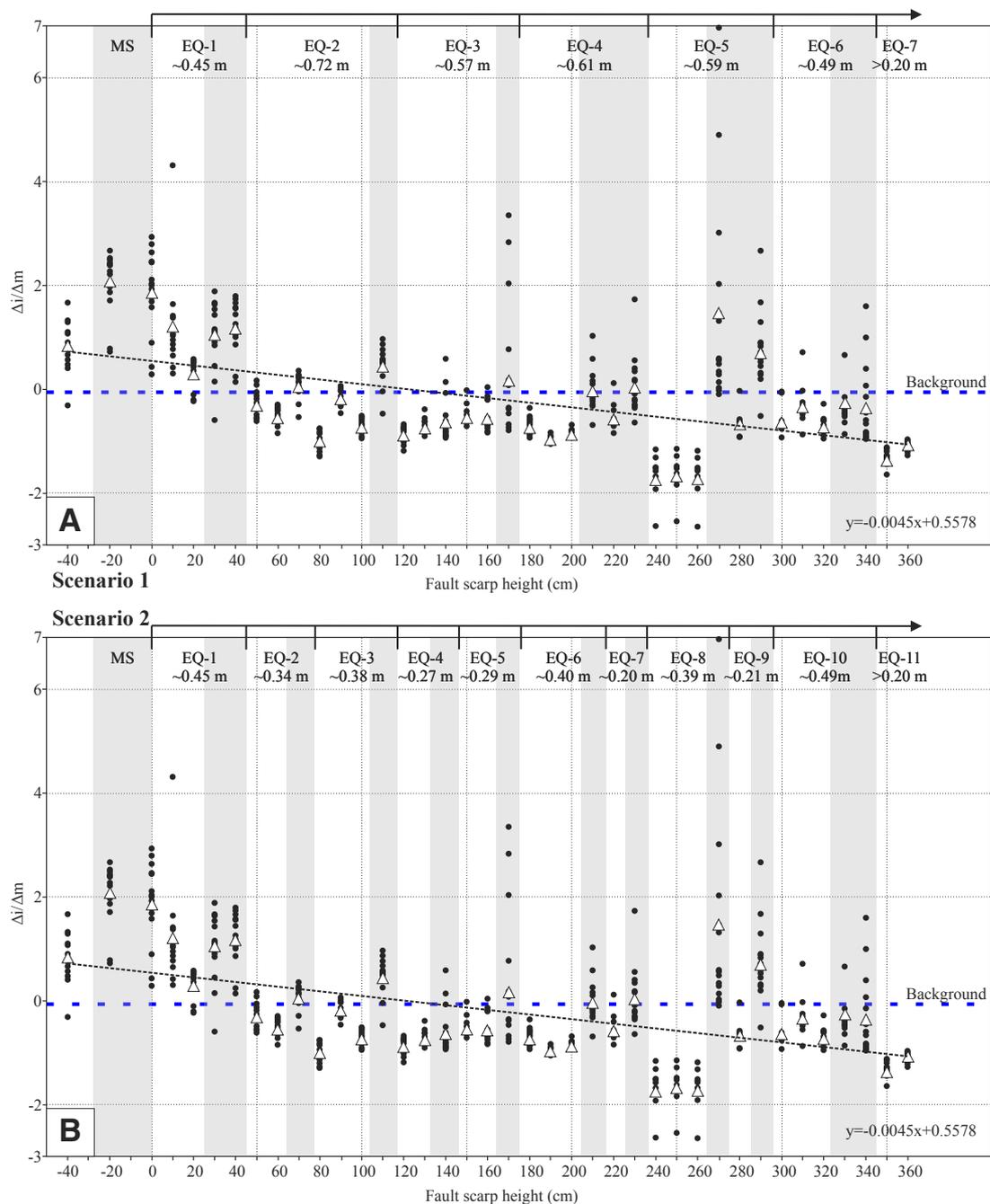
Figure 11. Variability of rare earth elements + Y (REE-Y) content in the 39 limestone sample cores as a function of fault scarp height (cm). Following Carcaillet et al. (2008), the vertical axis represents $\Delta i/\Delta m$, where Δi equals $Ci - Cm$, with Ci = concentration in each sample, and Cm = mean concentration over the whole sample suite, and Δm represents $\sum|\Delta i|/n$, which is the mean absolute value of the difference normalized to n (number of measurements = 39). The black dots represent each element of REE-Y, while the triangle indicates the average value of REE-Y. The gray line represents the average REE-Y content in the three Timpa limestone background samples, and the dashed black line is the linear regression of the data (the equation of the line is included in the figure). Shaded gray vertical rectangles highlight portions of the scarp that have been enriched in REE-Y. (A–B) The two different scenarios presented in the text. EQ—earthquake; MS—modern soil.

TABLE 4. RADIOCARBON AGES OF SAMPLES COLLECTED AT THE SAMPLING SITE SHOWN IN FIGURE S2
(DEPOSITS CUT BY THE FAULT PLANE SAMPLED FOR GEOCHEMICAL ANALYSES)

Sample	Laboratory	Analysis	Dated material	$\delta^{13}C$ (‰)	Conventional radiocarbon age (yr B.P.)	Calibrated age range (2σ cal. yr B.P., 95%)
TDV18-01	Beta518964	AMS	Organic sediment	−24.2	9650 ± 30	11,185–10,800
TDV18-02	Beta518965	AMS	Organic sediment	−24.3	19,670 ± 70	23,695–23,380

Notes: AMS—accelerator mass spectrometry by Beta Analytic Inc., Miami, Florida. Samples were calibrated using the software CALIB 8.2 (Stuiver et al., 2021). See text footnote 1 for Figure S2.

Constraints on Surface Faulting

The results obtained from the analysis of the 39 cores acquired here (Figs. 1B, 2A, and 7) on the slickenside cropping out along the Timpa del Vento segment allowed us to obtain the concentrations of REE-Y contents in their up-scarp variation. Our data showed an enrichment and depletion in the up-scarp evolution of the REE-Y concentrations, with clear peaks along the scarp. The analyses also showed that the present soil is enriching the fault plane in contact with the soil (see Fig. 10). We also observed fractionation between LREE/HREE contents, which indicates that the greatest enrichment is due to the behavior of LREEs, while HREEs remain almost immobile during the exchange process at the soil-fault plane. In Figure 11, we show these concentrations along the fault plane, and, following the approach adopted by Carcaillet et al. (2008), Manighetti et al. (2010), and Mouslopoulou et al. (2011), we identified sections that could be considered representative of seismic events or abrupt erosion phases that have occurred over time at least since the LGM. In particular, we considered at least two different scenarios, one with seven higher-magnitude earthquakes, and another with 11 lower-magnitude earthquakes. We underline that since both scenarios have in common the total displacement of the scarp, they should be considered equivalent in terms of total energy release; moreover, they just represent the extremes of what might have happened, whereas mixtures of the two are not excluded. The substantial difference is that, in the first case, we only considered the major enrichments as representing phases of contact between the soil and the fault plane, while in the second scenario, we highlighted each enrichment peak. Each earthquake is represented by the portion of the scarp that is enriched (gray areas in Fig. 11) plus the nonenriched portion (white area immediately before the gray one in Fig. 11) that has not been in contact with the soil due to the minimum and variable thickness of the soil itself. In fact, as shown in the conceptual model in Figure 5, each enriched fault plane portion should not be considered with respect to all the others, but only with respect to an immediately preceding non-enriched portion. The sum of them represents the thickness of the earthquake displacement. Although the methodology applied in this work might have potential perspective for the study of past earthquakes, the findings are subject to at least two assumptions that need to be acknowledged: (1) Each of the peaks obtained is coseismic and not due to slope erosion; (2) the earthquakes that can be counted represent the minimum number of earthquakes sourced by the fault, as highlighted by

Mouslopoulou et al. (2011). This latter statement is based in turn on the following three reasons: (2.1) Low- to moderate-magnitude earthquakes are not recorded because they did not rupture at the surface; (2.2) some earthquakes could have occurred temporally so close to each other as to not allow the soil to enrich the fault plane in REEs; and (2.3) some earthquakes may have had slip values less than the thickness of the soil. As far as assumption 1, as the fault activity and capability have been demonstrated by paleoseismological investigations (Galli et al., 2006), we feel confident that peaks could really be coseismic.

Implications for Seismic Potential

We speculated on the magnitude of the earthquakes that could have generated the exhumations of the fault plane as seen in Figure 11, considering different empirical relationships, which needed the maximum and average displacement as input data (i.e., Leonard, 2010; Thingbaijam et al., 2017; Wells and Coppersmith, 1994; Wesnousky, 2008). As shown in Table 5, we calculated the magnitudes for both scenarios in Figure 11, considering the *VS* obtained from the REE analysis both as average displacement and as maximum displacement (i.e., both for the empirical laws of Wells and Coppersmith [1994] and Wesnousky [2008] and only the average displacement for Leonard [2010] and Thingbaijam et al. [2017]). Obviously, this is an assumption, since, depending on the earthquake that generated it, the coseismic rupture that occurred at the measurement site may not represent the maximum or the average of the deformation. The result of the magnitudes can, however, be considered as a minimum, and therefore worthy of note. According to empirical laws, the observed displacements would account for earthquakes of $6.1 \leq M_w \leq 7.0$ for scenario 1 and for earthquakes of $5.5 \leq M_w \leq 6.7$ for scenario 2 (excluding Eq. 7 and Eq. 11 from scenario 1 and 2, respectively, which has a minimum *VS* of 20 cm but for which the maximum is unknown). Assuming an average of all the empirical laws for each earthquake, we estimate that the magnitude was always $6.1 \leq M_w \leq 6.7$ for scenario 1 and $6.1 \leq M_w \leq 6.5$ for scenario 2. Finally, regression curves offer an estimate of the most recurrent earthquake of $M_w = 6.6$ in scenario 1 and $M_w = 6.4$ in the case of scenario 2.

From the REE analysis, it is not possible to assign a time to the exhumation/faulting events. However, it is possible to constrain the number of supposed earthquakes within the post-LGM period, locally suggested by the radiocarbon

TABLE 5. EARTHQUAKE MAGNITUDES (M$_w$) FROM THE VERTICAL SEPARATION (*VS*) OBTAINED WITH RARE EARTH ELEMENT (REE) ANALYSIS OF THE FAULT PLANE AT THE SAMPLING SITE*

Earthquake number	VS (m)	Wells and Coppersmith (1994)		Wesnousky (2008)		Leonard (2010)		Thingbaijam et al. (2017)	
		Average *VS*	Max *VS*	Average *VS*	Max *VS*	Average *VS*	Max *VS*	Average *VS*	Max *VS*
Scenario 1									
Eq-1	0.45	6.6	6.4	6.7	6.5	6.1	–	6.7	–
Eq-2	0.72	6.7	6.5	6.8	6.5	6.5	–	7.0	–
Eq-3	0.57	6.6	6.4	6.7	6.5	6.3	–	6.8	–
Eq-4	0.61	6.6	6.5	6.7	6.5	6.4	–	6.9	–
Eq-5	0.59	6.6	6.5	6.7	6.5	6.4	–	6.8	–
Eq-6	0.49	6.6	6.4	6.7	6.5	6.2	–	6.7	–
Eq-7	>20	6.3	6.1	6.5	6.3	5.5	–	6.2	–
Scenario 2									
Eq-1	0.45	6.6	6.4	6.7	6.5	6.1	–	6.7	–
Eq-2	0.34	6.5	6.3	6.6	6.4	5.9	–	6.5	–
Eq-3	0.38	6.5	6.3	6.6	6.4	6.0	–	6.6	–
Eq-4	0.27	6.4	6.2	6.6	6.3	5.7	–	6.4	–
Eq-5	0.29	6.4	6.2	6.6	6.4	5.8	–	6.4	–
Eq-6	0.4	6.5	6.3	6.7	6.4	6.1	–	6.6	–
Eq-7	0.2	6.3	6.1	6.5	6.3	5.5	–	6.2	–
Eq-8	0.39	6.5	6.3	6.6	6.4	6.0	–	6.6	–
Eq-9	0.21	6.3	6.1	6.5	6.3	5.5	–	6.2	–
Eq-10	0.49	6.6	6.4	6.7	6.5	6.2	–	6.7	–
Eq-11	>20	6.3	6.1	6.5	6.3	5.5	–	6.2	–

*Obtained from the empirical equations of Leonard (2010), Thingbaijam et al. (2017), Wells and Coppersmith (1994), and Wesnousky (2008).

age of the truncated paleosol in the hanging wall (ca. 24 cal. k.y. B.P.; Table 4). Therefore, on one hand, an earthquake with an average M$_w$ = 6.6 would occur every 3.4 to 2.2 k.y. in scenario 1, while, on the other hand, an earthquake with an average M$_w$ = 6.4 would occur every ~2.2–1.5 k.y. Certainly, these calculations derive from the assumption of the maximum of the considered time (~24 k.y.), while it is likely that the observation time scale should be further restricted (less than 16 k.y., considering climatic flattening of the slope, which, according to Galli et al. [2006], ended ca. 16 ka, and the time needed for the soil to develop after the LGM). Nonetheless, many authors in the literature agree that faults may cluster earthquakes in frequent short periods, which then alternate with long periods of nonseismicity (e.g., Bull et al., 2006; Cowie et al., 2012, 2017; Galli et al., 2008; Mildon et al., 2022; Mouslopoulou et al., 2009; Romano et al., 2013; Wedmore et al., 2017; Zinke et al., 2018; among others). This would explain the supposed activation of the Caggiano-Montemurro fault in 1561 and again in 1857. A recurrence time between ~1.6 and ~2.5 k.y. is in the same order as the other known active faults of the Apenninic chain (Galli, 2000) as well as a slip rate, which, according to our results, ranges between ~0.6 and ~0.9 mm/yr. These values were obtained by measuring ~14 m (average) of cumulative offset across the fault (see previous sections and Fig. S1) that occurred after the climatic flattening of the slope (ended ca. 16 ka). Our results confirm previous findings, contribute to our understanding of faults and earthquakes from this portion of Italy, and provide an approach that should be useful worldwide.

REFERENCES CITED

Amicucci, L., Barchi, M.R., Montone, P., and Rubiliani, N., 2008, The Vallo di Diano and Auletta extensional basins in the Southern Apennines (Italy): A simple model for a complex setting: Terra Nova, v. 20, p. 475–482, https://doi.org/10.1111/j.1365-3121.2008.00841.x.
Andrenacci, C., Bello, S., Barbano, M.S., de Nardis, R., Pirrotta, C., Pietrolungo, F., and Lavecchia, G., 2023, Reappraisal and analysis of macroseismic data for seismotectonic purposes: The strong earthquakes of southern Calabria, Italy: Geosciences, v. 13, 212, https://doi.org/10.3390/geosciences13070212.

Auer, G., Hauzenberger, C.A., Reuter, M., and Piller, W.E., 2016, Orbitally paced phosphogenesis in Mediterranean shallow marine carbonates during the middle Miocene Monterey event: Geochemistry, Geophysics, Geosystems, v. 17, no. 4, p. 1492–1510, https://doi.org/10.1002/2016GC006299.

Balcaen, L., Bolea-Fernandez, E., Resano, M., and Vanhaecke, F., 2015, Inductively coupled plasma–tandem mass spectrometry (ICP-MS/MS): A powerful and universal tool for the interference-free determination of (ultra)trace elements—A tutorial review: Analytica Chimica Acta, v. 894, p. 7–19, https://doi.org/10.1016/j.aca.2015.08.053.

Barchi, M., Amato, A., Cippitelli, G., Merlini, S., and Montone, P., 2007, Extensional tectonics and seismicity in the axial zone of the Southern Apennines: Bollettino della Società Geologica Italiana, v. 7, Supplemento, p. 47–56.

Bello, S., de Nardis, R., Scarpa, R., Brozzetti, F., Cirillo, D., Ferrarini, F., di Lieto, B., Arrowsmith, J.R., and Lavecchia, G., 2021a, Fault pattern and seismotectonic style of the Campania-Lucania 1980 earthquake (Mw 6.9, southern Italy): New multidisciplinary constraints: Frontiers of Earth Science, v. 8, https://doi.org/10.3389/feart.2020.608063.

Bello, S., Scott, C.P., Ferrarini, F., Brozzetti, F., Scott, T., Cirillo, D., de Nardis, R., Arrowsmith, J.R., and Lavecchia, G., 2021b, High-resolution surface faulting from the 1983 Idaho Lost River fault Mw 6.9 earthquake and previous events: Scientific Data, v. 8, no. 1, p. 68, https://doi.org/10.1038/s41597-021-00838-6.

Bello, S., Andrenacci, C., Cirillo, D., Scott, C.P., Brozzetti, F., Arrowsmith, J.R., and Lavecchia, G., 2022a, High-detail fault segmentation: Deep insight into the anatomy of the 1983 Borah Peak earthquake rupture zone (Mw 6.9, Idaho, USA): Lithosphere, v. 2022, no. 1, https://doi.org/10.2113/2022/8100224.

Bello, S., Lavecchia, G., Andrenacci, C., Ercoli, M., Cirillo, D., Carboni, F., Barchi, M.R., and Brozzetti, F., 2022b, Complex trans-ridge normal faults controlling large earthquakes: Scientific Reports, v. 12, no. 1, 10676, https://doi.org/10.1038/s41598-022-14406-4.

Benedetti, L., Finkel, R., Papanastassiou, D., King, G., Armijo, R., Ryerson, F., Farber, D., and Flerit, F., 2002, Post-glacial slip history of the Sparta fault (Greece) determined by ^{36}Cl cosmogenic dating: Evidence for non-periodic earthquakes: Geophysical Research Letters, v. 29, no. 8, p. 87-81–87-84, https://doi.org/10.1029/2001GL014510.

Benedetti, L., Manighetti, I., Gaudemer, Y., Finkel, R., Malavieille, J., Pou, K., Arnold, M., Aumaître, G., Bourlès, D., and Keddadouche, K., 2013, Earthquake synchrony and clustering on Fucino faults (central Italy) as revealed from in situ ^{36}Cl exposure dating: Journal of Geophysical Research: Solid Earth, v. 118, no. 9, p. 4948–4974, https://doi.org/10.1002/jgrb.50299.

Bolkas, D., 2019, Assessment of GCP number and separation distance for small UAS surveys with and without GNSS-PPK positioning: Journal of Surveying Engineering, v. 145, no. 3, https://doi.org/10.1061/(ASCE)SU.1943-5428.0000283.

Brozzetti, F., 2011, The Campania-Lucania extensional fault system, southern Italy: A suggestion for a uniform model of active extension in the Italian Apennines: Tectonics, v. 30, TC5009, https://doi.org/10.1029/2010TC002794.

Brozzetti, F., and Salvatore, A., 2005, Quaternary extensional fault-systems from Northern and Southern Apennines: Similarities and differences: Rendiconti Online della Società Geologica Italiana, v. 1, p. 58–60.

Brozzetti, F., Lavecchia, G., Mancini, G., Milana, G., and Cardinali, M., 2009, Analysis of the 9 September 1998 Mw 5.6 Mercure earthquake sequence (Southern Apennines, Italy): A multidisciplinary approach: Tectonophysics, v. 476, p. 210–225, https://doi.org/10.1016/j.tecto.2008.12.007.

Brozzetti, F., Cirillo, D., de Nardis, R., Cardinali, M., Lavecchia, G., Orecchio, B., Presti, D., and Totaro, C., 2017a, Newly identified active faults in the Pollino seismic gap, southern Italy, and their seismotectonic significance: Journal of Structural Geology, v. 94, p. 13–31, https://doi.org/10.1016/j.jsg.2016.10.005.

Brozzetti, F., Cirillo, D., Liberi, F., Piluso, E., Faraca, E., De Nardis, R., and Lavecchia, G., 2017b, Structural style of Quaternary extension in the Crati Valley (Calabrian arc): Evidence in support of an east-dipping detachment fault: Italian Journal of Geosciences, v. 136, p. 434–453, https://doi.org/10.3301/IJG.2017.11.

Brozzetti, F., Boncio, P., Cirillo, D., Ferrarini, F., de Nardis, R., Testa, A., Liberi, F., and Lavecchia, G., 2019, High-resolution field mapping and analysis of the August–October 2016 coseismic surface faulting (central Italy earthquakes): Slip distribution, parameterization, and comparison with global earthquakes: Tectonics, v. 38, p. 417–439, https://doi.org/10.1029/2018TC005305.

Brozzetti, F., Mondini, A.C., Pauselli, C., Mancinelli, P., Cirillo, D., Guzzetti, F., and Lavecchia, G., 2020, Mainshock anticipated by intra-sequence ground deformations: Insights from multiscale field and SAR interferometric measurements: Geosciences, v. 10, https://doi.org/10.3390/geosciences10050186.

Bubeck, A., Wilkinson, M., Roberts, G.P., Cowie, P.A., McCaffrey, K.J.W., Phillips, R., and Sammonds, P., 2015, The tectonic geomorphology of bedrock scarps on active normal faults in the Italian Apennines mapped using combined ground penetrating radar and terrestrial laser scanning: Geomorphology, v. 237, p. 38–51, https://doi.org/10.1016/j.geomorph.2014.03.011.

Bucci, F., Cardinali, M., and Guzzetti, F., 2013, Structural geomorphology, active faulting and slope deformations in the epicentre area of the MW 7.0, 1857, southern Italy earthquake: Physics and Chemistry of the Earth, v. 63, p. 12–24, https://doi.org/10.1016/j.pce.2013.04.005.

Bucci, F., Novellino, R., Guglielmi, P., and Tavarnelli, E., 2020, Growth and dissection of a fold and thrust belt: The geological record of the High Agri Valley, Italy: Journal of Maps, v. 16, p. 245–256, https://doi.org/10.1080/17445647.2020.1737254.

Bull, J.M., Barnes, P.M., Lamarche, G., Sanderson, D.J., Cowie, P.A., Taylor, S.K., and Dix, J.K., 2006, High-resolution record of displacement accumulation on an active normal fault: Implications for models of slip accumulation during repeated earthquakes: Journal of Structural Geology, v. 28, no. 7, p. 1146–1166, https://doi.org/10.1016/j.jsg.2006.03.006.

Cao, X., Chen, Y., Wang, X., and Deng, X., 2001, Effects of redox potential and pH value on the release of rare earth elements from soil: Chemosphere, v. 44, p. 655–661, https://doi.org/10.1016/S0045-6535(00)00492-6.

Carcaillet, J., Manighetti, I., Chauvel, C., Schlagenhauf, A., and Nicole, J.-M., 2008, Identifying past earthquakes on an active normal fault (Magnola, Italy) from the chemical analysis of its exhumed carbonate fault plane: Earth and Planetary Science Letters, v. 271, p. 145–158, https://doi.org/10.1016/j.epsl.2008.03.059.

Casciello, E., Cesarano, M., and Pappone, G., 2006, Extensional detachment faulting on the Tyrrhenian margin of the Southern Apennines contractional belt (Italy): Journal of the Geological Society, v. 163, p. 617–629, https://doi.org/10.1144/0016-764905-054.

Castaldo, R., de Nardis, R., DeNovellis, V., Ferrarini, F., Lanari, R., Lavecchia, G., Pepe, S., Solaro, G., and Tizzani, P., 2018, Coseismic stress and strain field changes investigation through 3-D finite element modeling of DInSAR and GPS measurements and geological/seismological data: The L'Aquila (Italy) 2009 earthquake case study: Journal of Geophysical Research: Solid Earth, v. 123, p. 4193–4222, https://doi.org/10.1002/2017JB014453.

Castelli, V., Galli, P., Camassi, R., and Caracciolo, C., 2008, The 1561 earthquake(s) in southern Italy: New insights into a complex seismic sequence: Journal of Earthquake Engineering, v. 12, no. 7, p. 1054–1077, https://doi.org/10.1080/13632460801890356.

Cello, G., Tondi, E., Micarelli, L., and Mattioni, L., 2003, Active tectonics and earthquake sources in the epicentral area of the 1857 Basilicata earthquake (southern Italy): Journal of Geodynamics, v. 36, no. 1–2, p. 37–50, https://doi.org/10.1016/S0264-3707(03)00037-1.

Chen, J., Blume, H.-P., and Beyer, L., 2000, Weathering of rocks induced by lichen colonization—A review: Catena, v. 39, p. 121–146, https://doi.org/10.1016/S0341-8162(99)00085-5.

Cirillo, D., 2020, Digital field mapping and drone-aided survey for structural geological data collection and seismic hazard assessment: Case of the 2016 central Italy earthquakes: Applied Sciences (Switzerland), v. 10, https://doi.org/10.3390/app10155233.

Cirillo, D., Cerritelli, F., Agostini, S., Bello, S., Lavecchia, G., and Brozzetti, F., 2022a, Integrating post-processing kinematic (PPK)–structure-from-motion (SfM) with unmanned aerial vehicle (UAV): Photogrammetry and digital field mapping for structural geological analysis: ISPRS International Journal of Geo-Information, v. 11, no. 8, https://doi.org/10.3390/ijgi11080437.

Cirillo, D., Totaro, C., Lavecchia, G., Orecchio, B., de Nardis, R., Presti, D., Ferrarini, F., Bello, S., and Brozzetti, F., 2022b, Structural complexities and tectonic barriers controlling recent seismic activity in the Pollino area (Calabria-Lucania, southern Italy)—Constraints from stress inversion and 3D fault model building: Solid Earth, v. 13, no. 1, p. 205–228, https://doi.org/10.5194/se-13-205-2022.

Civico, R., Pucci, S., Villani, F., Pizzimenti, L., De Martini, P.M., Nappi, R., and the Open EMER-GEO Working Group, 2018, Surface ruptures following the 30 October 2016 Mw 6.5 Norcia earthquake, central Italy: Journal of Maps, v. 14, no. 2, p. 151–160, https://doi.org/10.1080/17445647.2018.1441756.

Cledat, E., Jospin, L.V., Cucci, D.A., and Skaloud, J., 2020, Mapping quality prediction for RTK/PPK-equipped micro-drones operating in complex natural environment: ISPRS Journal of Photogrammetry and Remote Sensing, v. 167, p. 24–38, https://doi.org/10.1016/j.isprsjprs.2020.05.015.

Cowie, P., Roberts, G., Bull, J.M., and Visini, F., 2012, Relationships between fault geometry, slip rate variability and earthquake recurrence in extensional settings: Geophysical Journal International, v. 189, p. 143–160, https://doi.org/10.1111/j.1365-246X.2012.05378.x.

Cowie, P., Phillips, R., Roberts, G., McCaffrey, K., Zijerveld, L.J.J., Gregory, L.C., Faure Walker, J., Wedmore, L.N.J., Dunai, T.J., Binnie, S.A., Freeman, S.P.H.T., and Wilcken, K., 2017, Orogen-scale uplift in the central Italian Apennines drives episodic behaviour of earthquake faults: Scientific Reports, v. 7, https://doi.org/10.1038/srep44858.

Cucci, L., 2022, NW-dipping versus SE-dipping causative faults of the 1783 M 7.1 southern Calabria (Italy) earthquake: The contribution from the analysis of the coseismic hydrological changes: Frontiers of Earth Science, v. 10, https://doi.org/10.3389/feart.2022.987731.

de Nardis, R., Pandolfi, C., Cattaneo, M., Monachesi, G., Cirillo, D., Ferrarini, F., Bello, S., Brozzetti, F., and Lavecchia, G., 2022, Lithospheric double shear zone unveiled by microseismicity in a region of slow deformation: Scientific Reports, v. 12, 21066, https://doi.org/10.1038/s41598-022-24903-1.

Di Giulio, G., de Nardis, R., Boncio, P., Milana, G., Rosatelli, G., Stoppa, F., and Lavecchia, G., 2016, Seismic response of a deep continental basin including velocity inversion: The Sulmona intramontane basin (Central Apennines, Italy): Geophysical Journal International, v. 204, p. 418–439, https://doi.org/10.1093/gji/ggv444.

Di Luccio, F., Fukuyama, E., and Pino, N.A., 2005, The 2002 Molise earthquake sequence: What can we learn about the tectonics of southern Italy?: Tectonophysics, v. 405, no. 1–4, p. 141–154, https://doi.org/10.1016/j.tecto.2005.05.024.

Di Naccio, D., Boncio, P., Brozzetti, F., Pazzaglia, F.J., and Lavecchia, G., 2013, Morphotectonic analysis of the Lunigiana and Garfagnana grabens (Northern Apennines, Italy): Implications for active normal faulting: Geomorphology, v. 201, p. 293–311, https://doi.org/10.1016/j.geomorph.2013.07.003.

DuRoss, C.B., Bunds, M.P., Gold, R.D., Briggs, R.W., Reitman, N.G., Personius, S.F., and Toké, N.A., 2019, Variable normal-fault rupture behavior, northern Lost River fault zone, Idaho, USA: Geosphere, v. 15, p. 1869–1892, https://doi.org/10.1130/GES02096.1.

Ferrarini, F., Lavecchia, G., de Nardis, R., and Brozzetti, F., 2015, Fault geometry and active stress from earthquakes and field geology data analysis: The Colfiorito 1997 and L'Aquila 2009 cases (central Italy): Pure and Applied Geophysics, v. 172, p. 1079–1103, https://doi.org/10.1007/s00024-014-0931-7.

Galadini, F., and Galli, P., 2000, Active tectonics in the Central Apennines (Italy)—Input data for seismic hazard assessment: Natural Hazards, v. 22, p. 225–268, https://doi.org/10.1023/A:1008149531980.

Galli, P., 2000, New empirical relationships between magnitude and distance for liquefaction: Tectonophysics, v. 324, p. 169–187, https://doi.org/10.1016/S0040-1951(00)00118-9.

Galli, P., 2020, Recurrence times of Central-Southern Apennine faults (Italy): Hints from palaeoseismology: Terra Nova, v. 32, p. 399–407, https://doi.org/10.1111/ter.12470.

Galli, P., and Bosi, V., 2003, Catastrophic 1638 earthquakes in Calabria (southern Italy): New insights from paleoseismological investigation: Journal of Geophysical Research: Solid Earth, v. 108, p. 1–20, https://doi.org/10.1029/2001JB001713.

Galli, P., and Peronace, E., 2014, New paleoseismic data from the Irpinia fault: A different seismogenic perspective for Southern Apennines (Italy): Earth-Science Reviews, v. 136, p. 175–201, https://doi.org/10.1016/j.earscirev.2014.05.013.

Galli, P., Bosi, V., Piscitelli, S., Giocoli, A., and Scionti, V., 2006, Late Holocene earthquakes in Southern Apennines: Paleoseismology of the Caggiano fault: International Journal of Earth Sciences, v. 95, p. 855–870, https://doi.org/10.1007/s00531-005-0066-2.

Galli, P., Galadini, F., and Pantosti, D., 2008, Twenty years of paleoseismology in Italy: Earth-Science Reviews, v. 88, p. 89–117, https://doi.org/10.1016/j.earscirev.2008.01.001.

Galli, P., Messina, P., Giaccio, B., Peronace, E., and Quadrio, B., 2012, Early Pleistocene to late Holocene activity of the Magnola fault (Fucino fault system, central Italy): Bollettino di Geofisica Teorica ed Applicata, v. 53, no. 4, p. 435–458, https://doi.org/10.4430/bgta0054.

Galli, P., Giaccio, B., Messina, P., Peronace, E., Amato, V., Naso, G., Nomade, S., Pereira, A., Piscitelli, S., Bellanova, J., Billi, A., Blamart, D., Galderisi, A., Giocoli, A., Stabile, T., and Thil, F., 2017, Middle to late Pleistocene activity of the northern Matese fault system (Southern Apennines, Italy): Tectonophysics, v. 699, p. 61–81, https://doi.org/10.1016/j.tecto.2017.01.007.

Galli, P., Galderisi, A., Messina, P., and Peronace, E., 2022, The Gran Sasso fault system: Paleoseismological constraints on the catastrophic 1349 earthquake in central Italy: Tectonophysics, v. 822, https://doi.org/10.1016/j.tecto.2021.229156.

Giano, S.I., Maschio, L., Alessio, M., Ferranti, L., Improta, S., and Schiattarella, M., 2000, Radiocarbon dating of active faulting in the Agri High Valley, southern Italy: Journal of Geodynamics, v. 29, p. 371–386, https://doi.org/10.1016/S0264-3707(99)00058-7.

Gori, S., Giaccio, B., Galadini, F., Falcucci, E., Messina, P., Sposato, A., and Dramis, F., 2011, Active normal faulting along the Mt. Morrone south-western slopes (Central Apennines, Italy):

International Journal of Earth Sciences, v. 100, p. 157–171, https://doi.org/10.1007/s00531-009-0505-6.

Herrmann, R.B., Malagnini, L., and Munafò, I., 2011, Regional moment tensors of the 2009 l'Aquila earthquake sequence: Bulletin of the Seismological Society of America, v. 101, p. 975–993, https://doi.org/10.1785/0120100184.

Iezzi, F., Roberts, G., Faure Walker, J., Papanikolaou, I., Ganas, A., Deligiannakis, G., Beck, J., Wolfers, S., and Gheorghiu, D., 2021, Temporal and spatial earthquake clustering revealed through comparison of millennial strain-rates from ³⁶Cl cosmogenic exposure dating and decadal GPS strain-rate: Scientific Reports, v. 11, https://doi.org/10.1038/s41598-021-02131-3.

James, M.R., and Robson, S., 2012, Straightforward reconstruction of 3D surfaces and topography with a camera: Accuracy and geoscience application: Journal of Geophysical Research: Earth Surface, v. 117, p. 1–17, https://doi.org/10.1029/2011JF002289.

Johnson, K., Nissen, E., Saripalli, S., Arrowsmith, J.R., McGarey, P., Scharer, K., Williams, P., and Blisniuk, K., 2014, Rapid mapping of ultrafine fault zone topography with structure from motion: Geosphere, v. 10, p. 969–986, https://doi.org/10.1130/GES01017.1.

Kabata-Pendias, A., 2010, Trace Elements in Soils and Plants (4th edition): Boca Raton, Florida, Taylor & Francis Group, CRC Press, 548 p.

Lavecchia, G., 1988, The Tyrrhenian-Apennines system: Structural setting and seismotectogenesis: Tectonophysics, v. 147, no. 3–4, p. 263–296, https://doi.org/10.1016/0040-1951(88)90190-4.

Lavecchia, G., Brozzetti, F., Barchi, M., Menichetti, M., and Keller, J.V.A., 1994, Seismotectonic zoning in east-central Italy deduced from an analysis of the Neogene to present deformations and related stress fields: Geological Society of America Bulletin, v. 106, p. 1107–1120, https://doi.org/10.1130/0016-7606(1994)106<1107:SZIECI>2.3.CO;2.

Lavecchia, G., Adinolfi, G.M., de Nardis, R., Ferrarini, F., Cirillo, D., Brozzetti, F., De Matteis, R., Festa, G., and Zollo, A., 2017, Multidisciplinary inferences on a newly recognized active east-dipping extensional system in central Italy: Terra Nova, v. 29, p. 77–89, https://doi.org/10.1111/ter.12251.

Lavecchia, G., de Nardis, R., Ferrarini, F., Cirillo, D., Bello, S., and Brozzetti, F., 2021, Regional seismotectonic zonation of hydrocarbon fields in active thrust belts: A case study from Italy, in Bonali, F.L., Mariotto F.P., and Tsereteli, N., eds., Building Knowledge for Geohazard Assessment and Management in the Caucasus and other Orogenic Regions: Dordrecht, Netherlands, Springer, p. 89–128, https://doi.org/10.1007/978-94-024-2046-3_7.

Lavecchia, G., Bello, S., Andrenacci, C., Cirillo, D., Ferrarini, F., Vicentini, N., de Nardis, R., Roberts, G., and Brozzetti, F., 2022, Quaternary fault strain indicators database: QUIN 1.0—First release from the Apennines of central Italy: Scientific Data, v. 9, no. 1, p. 204, https://doi.org/10.1038/s41597-022-01311-8.

Leonard, M., 2010, Earthquake fault scaling: Self-consistent relating of rupture length, width, average displacement, and moment release: Bulletin of the Seismological Society of America, v. 100, no. 5A, p. 1971–1988, https://doi.org/10.1785/0120090189.

López-Comino, J.Á., Braun, T., Dahm, T., Cesca, S., and Danesi, S., 2021, On the source parameters and genesis of the 2017, Mw 4 Montesano earthquake in the outer border of the Val d'Agri oilfield (Italy): Frontiers of Earth Science, v. 8, https://doi.org/10.3389/feart.2020.617794.

Lucchetti, L., 1943, Rinvenimento di un deposito pliocenico marino nella zona delle Murge Nere (S. Angelo le Fratte, PZ): Bollettino della Società Geologica Italiana, v. 62, p. 39–40.

Madhavaraju, J., Loser, H., Lee, Y.I., Santacruz, R.L., and Pi-Puig, T., 2016, Geochemistry of Lower Cretaceous limestones of the Alisitos Formation, Baja California, Mexico: Implications for REE source and paleo-redox conditions: Journal of South American Earth Sciences, v. 66, p. 149–165, https://doi.org/10.1016/j.jsames.2015.11.013.

Manighetti, I., Campillo, M., Bouley, S., and Cotton, F., 2007, Earthquake scaling, fault segmentation, and structural maturity: Earth and Planetary Science Letters, v. 253, p. 429–438, https://doi.org/10.1016/j.epsl.2006.11.004.

Manighetti, I., Zigone, D., Campillo, M., and Cotton, F., 2009, Self-similarity of the largest-scale segmentation of the faults: Implications for earthquake behavior: Earth and Planetary Science Letters, v. 288, p. 370–381, https://doi.org/10.1016/j.epsl.2009.09.040.

Manighetti, I., Boucher, E., Chauvel, C., Schlagenhauf, A., and Benedetti, L., 2010, Rare earth elements record past earthquakes on exhumed limestone fault planes: Terra Nova, v. 22, no. 6, p. 477–482, https://doi.org/10.1111/j.1365-3121.2010.00969.x.

Mariucci, M.T., and Montone, P., 2016, Contemporary stress field in the area of the 2016 Amatrice seismic sequence (central Italy): Annals of Geophysics, v. 59, https://doi.org/10.4401/ag-7235.

Mildon, Z.K., Roberts, G.P., Faure Walker, J.P., Joakim, B., Papanikolaou, I., Michetti, A.M., Toda, S., Iezzi, F., Campbell, L., McCaffrey, K.J.W., Shanks, R., and Sgambato, C., 2022, Surface faulting

earthquake clustering controlled by fault and shear-zone interactions: Nature Communications, v. 13, p. 7126, https://doi.org/10.1038/s41467-022-34821-5.

Mirabella, F., Brozzetti, F., Lupattelli, A., and Barchi, M.R., 2011, Tectonic evolution of a low-angle extensional fault system from restored cross-sections in the Northern Apennines (Italy): Tectonics, v. 30, https://doi.org/10.1029/2011TC002890.

Mostardini, F., and Merlini, S., 1986, Appennino centro-meridionale: Sezioni geologiche e proposta di modello strutturale.pdf: Memorie della Società Geologica Italiana, v. 35, p. 177–202.

Mouslopoulou, V., Walsh, J.J., and Nicol, A., 2009, Fault displacement rates on a range of times-cales: Earth and Planetary Science Letters, v. 278, no. 3–4, p. 186–197, https://doi.org/10.1016/j.epsl.2008.11.031.

Mouslopoulou, V., Moraetis, D., and Fassoulas, C., 2011, Identifying past earthquakes on carbon-ate faults: Advances and limitations of the 'rare earth element' method based on analysis of the Spili fault, Crete, Greece: Earth and Planetary Science Letters, v. 309, no. 1–2, p. 45–55, https://doi.org/10.1016/j.epsl.2011.06.015.

Napolitano, F., Galluzzo, D., Gervasi, A., Scarpa, R., and La Rocca, M., 2021, Fault imaging at Mt. Pollino (Italy) from relative location of microearthquakes: Geophysical Journal International, v. 224, no. 1, p. 637–648, https://doi.org/10.1093/gji/ggaa407.

Neri, G., Orecchio, B., Scolaro, S., and Totaro, C., 2020, Major earthquakes of southern Calabria, Italy, into the regional geodynamic context: Frontiers in Earth Science, v. 8, https://doi.org/10.3389/feart.2020.579846.

Nicolai, C., and Gambini, R., 2007, Structural architecture of the Adria platform-and-basin system: Bollettino della Società Geologica Italiana, v. 7, Supplemento, p. 21–37.

Palumbo, L., Benedetti, L., Bourlès, D., Cinque, A., and Finkel, R., 2004, Slip history of the Magnola fault (Apennines, central Italy) from ³⁶Cl surface exposure dating: Evidence for strong earth-quakes over the Holocene: Earth and Planetary Science Letters, v. 225, no. 1–2, p. 163–176, https://doi.org/10.1016/j.epsl.2004.06.012.

Papanikolaou, I.D., and Roberts, G.P., 2007, Geometry, kinematics and deformation rates along the active normal fault system in the Southern Apennines: Implications for fault growth: Journal of Structural Geology, v. 29, no. 1, p. 166–188, https://doi.org/10.1016/j.jsg.2006.07.009.

Pescatore, T., Sgrosso, I., and Torre, M., 1970, Lineamenti di tettonica e sedimentazione nel Miocene dell'Appennino campano-lucano: Bollettino della Società dei Naturalisti in Napoli, Supple-mento, v. 78, p. 337–408.

Pescatore, T., Renda, P., Schiattarella, M., and Tramutoli, M., 1999, Stratigraphic and structural relationships between Meso-Cenozoic Lagonegro basin and coeval carbonate platforms in Southern Apennines, Italy: Tectonophysics, v. 315, p. 269–286, https://doi.org/10.1016/S0040-1951(99)00278-4.

Pondrelli, S., Salimbeni, S., Ekström, G., Morelli, A., Gasperini, P., and Vannucci, G., 2006, The Italian CMT dataset from 1977 to the present: Physics of the Earth and Planetary Interiors, v. 159, p. 286–303, https://doi.org/10.1016/j.pepi.2006.07.008.

Pondrelli, S., Visini, F., Rovida, A., D'Amico, V., Pace, B., and Meletti, C., 2020, Style of faulting of expected earthquakes in Italy as an input for seismic hazard modeling: Natural Hazards and Earth System Sciences, v. 20, no. 12, p. 3577–3592, https://doi.org/10.5194/nhess-20-3577-2020.

Pourret, O., Davranche, M., Gruau, G., and Dia, A., 2007, Rare earth elements complexation with humic acid: Chemical Geology, v. 243, p. 128–141, https://doi.org/10.1016/j.chemgeo.2007.05.018.

Pousse-Beltran, L., Benedetti, L., Fleury, J., Boncio, P., Guillou, V., Pace, B., Rizza, M., Puliti, I., and Socquet, A., 2022, ³⁶Cl exposure dating of glacial features to constrain the slip rate along the Mt. Vettore fault (Central Apennines, Italy): Geomorphology, v. 412, https://doi.org/10.1016/j.geomorph.2022.108302.

Roberts, G.P., and Michetti, A.M., 2004, Spatial and temporal variations in growth rates along active normal fault systems: An example from the Lazio-Abruzzo Apennines, central Italy: Journal of Structural Geology, v. 26, p. 339–376, https://doi.org/10.1016/S0191-8141(03)00103-2.

Robustelli, G., Ermolli, E.R., Petrosino, P., Jicha, B., Sardella, R., and Donato, P., 2014, Tectonic and climatic control on geomorphological and sedimentary evolution of the Mercure basin, Southern Apennines, Italy: Geomorphology, v. 214, p. 423–435, https://doi.org/10.1016/j.geomorph.2014.02.026.

Romano, M.A., De Nardis, R., Lavecchia, G., Garbin, M., Peruzza, L., Priolo, E., Romanelli, M., and Ferrarini, F., 2013, Preliminary analysis of the microearthquakes-faults association in the Sulmona basin (Central Apennines, Italy): Rendiconti Online Societa Geologica Italiana, v. 29, p. 150–153.

Rosatelli, G., Wall, F., Stoppa, F., and Brilli, M., 2010, Geochemical distinctions between igneous carbonate, calcite cements, and limestone xenoliths (Polino carbonatite, Italy): Spatially resolved LAICPMS analyses: Contributions to Mineralogy and Petrology, v. 160, p. 645–661, https://doi.org/10.1007/s00410-010-0499-x.

Rosatelli, G., Castorina, F., Consalvo, A., Brozzetti, F., Ciavardelli, D., Perna, M.G., Bell, K., Bello, S., and Stoppa, F., 2023, Elemental abundances and isotopic composition of Italian limestones: Glimpses into the evolution of the Tethys: Journal of Asian Earth Sciences, v. 9, https://doi.org/10.1016/j.jaesx.2023.100136.

Rovida, A., Locati, M., Camassi, R., Lolli, B., and Gasperini, P., 2020, The Italian earthquake cata-logue CPTI15: Bulletin of Earthquake Engineering, v. 18, no. 7, p. 2953–2984, https://doi.org/10.1007/s10518-020-00818-y.

Rovida, A., Locati, M., Camassi, R., Lolli, B., Gasperini, P., and Antonucci, A., 2022, Catalogo Parametrico dei Terremoti Italiani (CPTI15), Versione 4.0: Istituto Nazionale di Geofisica e Vul-canologia (INGV), https://emidius.mi.ingv.it/CPTI15-DBMI15/ (last accessed 23 February 2023).

Schiattarella, M., 1998, Quaternary tectonics of the Pollino Ridge, Calabria-Lucania boundary, southern Italy, in Holdsworth, R.E., et al., eds., Continental Transpressional and Transten-sional Tectonics: Geological Society, London, Special Publication 135, p. 341–354, https://doi.org/10.1144/GSL.SP.1998.135.01.22.

Schirripa Spagnolo, G., Mercuri, M., Billi, A., Carminati, E., and Galli, P., 2021, The segmented Campo Felice normal faults: Seismic potential appraisal by application of empirical relation-ships between rupture length and earthquake magnitude in the Central Apennines, Italy: Tectonics, v. 40, no. 7, https://doi.org/10.1029/2020TC006465.

Schlagenhauf, A., Manighetti, I., Benedetti, L., Gaudemer, Y., Finkel, R., Malavieille, J., and Pou, K., 2011, Earthquake supercycles in central Italy, inferred from ³⁶Cl exposure dating: Earth and Planetary Science Letters, v. 307, p. 487–500, https://doi.org/10.1016/j.epsl.2011.05.022.

Scognamiglio, L., Tinti, E., and Quintiliani, M., 2006, Time Domain Moment Tensor (TDMT): Istituto Nazionale di Geofisica e Vulcanologia (INGV), https://doi.org/10.13127/tdmt (last accessed 23 February 2023).

Scott, C.P., Bello, S., and Ferrarini, F., 2020, Matlab Algorithm for Systematic Vertical Separa-tion Measurements of Tectonic Fault Scarps: Zenodo, https://zenodo.org/record/4247586 (last accessed 20 December 2022).

Scott, C.P., Giampietro, T., Brigham, C., Leclerc, F., Manighetti, I., Arrowsmith, J.R., Laó-Dávila, D.A., Mattéo, L., and Chevalier, M.-L., 2022, Semiautomatic algorithm to map tectonic faults and measure scarp height from topography applied to the Volcanic Tablelands and the Hurricane fault, western US: Lithosphere, v. 2021, https://doi.org/10.2113/2021/9031662.

Scrocca, D., Sciamanna, S., Di Luzio, E., Tozi, M., Nicolai, C., and Gambini, R., 2007, Structural setting along the CROP-04 deep seismic profile (Southern Apennines, Italy): Bollettino della Società Geologica Italiana, v. 7, Supplemento, p. 283–296.

Sgambato, C., Faure Walker, J.P., and Roberts, G.P., 2020, Uncertainty in strain-rate from field mea-surements of the geometry, rates and kinematics of active normal faults: Implications for seismic hazard assessment: Journal of Structural Geology, v. 131, https://doi.org/10.1016/j.jsg.2019.103934.

Soliva, R., Benedicto, A., Schultz, R.A., Maerten, L., and Micarelli, L., 2008, Displacement and interaction of normal fault segments branched at depth: Implications for fault growth and potential earthquake rupture size: Journal of Structural Geology, v. 30, p. 1288–1299, https://doi.org/10.1016/j.jsg.2008.07.005.

Spina, V., Tondi, E., Galli, P., Mazzoli, S., and Cello, G., 2008, Quaternary fault segmentation and interaction in the epicentral area of the 1561 earthquake (Mw = 6.4), Vallo di Diano, Southern Apennines, Italy: Tectonophysics, v. 453, p. 233–245, https://doi.org/10.1016/j.tecto.2007.06.012.

Stewart, N., Gaudemer, Y., Manighetti, I., Serreau, L., Vincendeau, A., Dominguez, S., Mattéo, L., and Malavieille, J., 2018, "3D_Fault_Offsets," a Matlab code to automatically measure lateral and vertical fault offsets in topographic data: Application to San Andreas, Owens Valley, and Hope faults: Journal of Geophysical Research: Solid Earth, v. 123, p. 815–835, https://doi.org/10.1002/2017JB014863.

Stoppa, F., Cirilli, S., Sorci, A., Broom-Fendley, S., Principe, C., Perna, M.G., and Rosatelli, G., 2021, Igneous and sedimentary 'limestones': The puzzling challenge of a converging classification, in Di Capua, A., et al., eds., Volcanic Processes in the Sedimentary Record: When Volcanoes Meet the Environment: Geological Society, London, Special Publication 520, p. 327–352, https://doi.org/10.1144/SP520-2021-120.

Stuiver, M., Reimer, P.J., and Reimer, R.W., 2021, CALIB 8.2: http://calib.org (last accessed 17 April62023).

Sun, S.s., and McDonough, W.F., 1989, Chemical and isotopic systematics of oceanic basalts: Implications for mantle composition and processes, in Saunders, A.D., and Norry, M.J., eds., Magmatism in the Ocean Basins: Geological Society, London, Special Publication 42, p. 313–345, https://doi.org/10.1144/GSL.SP.1989.042.01.19.

Tangari, A.C., Scarciglia, F., Piluso, E., Marinangeli, L., and Pompilio, L., 2018, Role of weathering of pillow basalt, pyroclastic input and geomorphic processes on the genesis of the Monte Cerviero upland soils (Calabria, Italy): Catena, v. 171, p. 299–315, https://doi.org/10.1016/j.catena.2018.07.015.

Tangari, A.C., Le Pera, E., Andò, S., Garzanti, E., Piluso, E., Marinangeli, L., and Scarciglia, F., 2021, Soil-formation in the central Mediterranean: Insight from heavy minerals: Catena, v. 197, https://doi.org/10.1016/j.catena.2020.104998.

Tesson, J., Pace, B., Benedetti, L., Visini, F., Delli Rocioli, M., Arnold, M., Aumaître, G., Bourlès, D.L., and Keddadouche, K., 2016, Seismic slip history of the Pizzalto fault (central Apennines, Italy) using in situ-produced ³⁶Cl cosmic ray exposure dating and rare earth element concentrations: Journal of Geophysical Research: Solid Earth, v. 121, no. 3, p. 1983–2003, https://doi.org/10.1002/2015JB012565.

Thingbaijam, K.K.S., Martin Mai, P., and Goda, K., 2017, New empirical earthquake source-scaling laws: Bulletin of the Seismological Society of America, v. 107, no. 5, p. 2225–2246, https://doi.org/10.1785/0120170017.

Tortorici, L., Monaco, C., Tansi, C., and Cocina, O., 1995, Recent and active tectonics in the Calabrian arc (southern Italy): Tectonophysics, v. 243, p. 37–55, https://doi.org/10.1016/0040-1951(94)00190-K.

Tyler, G., 2004, Rare earth elements in soil and plant systems—A review: Plant and Soil, v. 267, p. 191–206, https://doi.org/10.1007/s11104-005-4888-2.

Vezzani, L., Festa, A., and Ghisetti, F.C., 2010, Geology and Tectonic Evolution of the Central-Southern Apennines, Italy: Geological Society of America Special Paper 469, 58 p., https://doi.org/10.1130/2010.2469.

Vichi, G., Perna, M.G., Ambrosio, F., Rosatelli, G., Cirillo, D., Broom-Fendley, S., Vladykin, N.V., Zaccaria, D., and Stoppa, F., 2022, La Queglia carbonatitic melnöite: A notable example of an ultra-alkaline rock variant in Italy: Mineralogy and Petrology (in press), https://doi.org/10.1007/s00710-022-00792-0.

Villani, F., and Pierdominici, S., 2010, Late Quaternary tectonics of the Vallo di Diano basin (Southern Apennines, Italy): Quaternary Science Reviews, v. 29, p. 3167–3183, https://doi.org/10.1016/j.quascirev.2010.07.003.

Villani, F., et al., 2018, A database of the coseismic effects following the 30 October 2016 Norcia earthquake in central Italy: Scientific Data, v. 5, https://doi.org/10.1038/sdata.2018.49.

Villani, F., Sapia, V., Baccheschi, P., Civico, R., Di Giulio, G., Vassallo, M., Marchetti, M., and Pantosti, D., 2019, Geometry and structure of a fault-bounded extensional basin by integrating geophysical surveys and seismic anisotropy across the 30 October 2016 Mw 6.5 earthquake fault (central Italy): The Pian Grande di Castelluccio Basin: Tectonics, v. 38, p. 26–48, https://doi.org/10.1029/2018TC005205.

Wedmore, L.N.J., Faure Walker, J.P., Roberts, G.P., Sammonds, P.R., McCaffrey, K.J.W., and Cowie, P.A., 2017, A 667 year record of coseismic and interseismic Coulomb stress changes in central Italy reveals the role of fault interaction in controlling irregular earthquake recurrence intervals: Journal of Geophysical Research: Solid Earth, v. 122, p. 5691–5711, https://doi.org/10.1002/2017JB014054.

Wells, D.L., and Coppersmith, K.J., 1994, New empirical relationships among magnitude, rupture length, rupture width, rupture area, and surface displacement: Bulletin of the Seismological Society of America, v. 84, no. 4, p. 974–1002, https://doi.org/10.1785/BSSA0840040974.

Wesnousky, S.G., 2008, Displacement and geometrical characteristics of earthquake surface ruptures: Issues and implications for seismic-hazard analysis and the process of earthquake rupture: Bulletin of the Seismological Society of America, v. 98, p. 1609–1632, https://doi.org/10.1785/0120070111.

Westoby, M.J., Brasington, J., Glasser, N.F., Hambrey, M.J., and Reynolds, J.M., 2012, 'Structure-from-motion' photogrammetry: A low-cost, effective tool for geoscience applications: Geomorphology, v. 179, p. 300–314, https://doi.org/10.1016/j.geomorph.2012.08.021.

Wilkinson, M., Roberts, G.P., McCaffrey, K., Cowie, P.A., Faure Walker, J.P., Papanikolaou, I., Phillips, R.J., Michetti, A.M., Vittori, E., Gregory, L., Wedmore, L., and Watson, Z.K., 2015, Slip distributions on active normal faults measured from LiDAR and field mapping of geomorphic offsets: An example from L'Aquila, Italy, and implications for modelling seismic moment release: Geomorphology, v. 237, p. 130–141, https://doi.org/10.1016/j.geomorph.2014.04.026.

Wilkinson, M.W., Jones, R.R., Woods, C.E., Gilment, S.R., McCaffrey, K.J.W., Kokkalas, S., and Long, J.J., 2016, A comparison of terrestrial laser scanning and structure-from-motion photogrammetry as methods for digital outcrop acquisition: Geosphere, v. 12, no. 6, p. 1865–1880, https://doi.org/10.1130/GES01342.1.

Wolfe, F.D., Stahl, T.A., Villamor, P., and Lukovic, B., 2020, Short communication: A semiautomated method for bulk fault slip analysis from topographic scarp profiles: Earth Surface Dynamics, v. 8, p. 211–219, https://doi.org/10.5194/esurf-8-211-2020.

Zembo, I., Panzeri, L., Galli, A., Bersezio, R., Martini, M., and Sibilia, E., 2009, Quaternary evolution of the intermontane Val d'Agri Basin, Southern Apennines: Quaternary Research, v. 72, p. 431–442, https://doi.org/10.1016/j.yqres.2009.02.009.

Zhang, H., Aldana-Jague, E., Clapuyt, F., Wilken, F., Vanacker, V., and Van Oost, K., 2019, Evaluating the potential of post-processing kinematic (PPK) georeferencing for UAV-based structure-from-motion (SfM) photogrammetry and surface change detection: Earth Surface Dynamics, v. 7, no. 3, p. 807–827, https://doi.org/10.5194/esurf-7-807-2019.

Zinke, R., Dolan, J.F., Rhodes, E.J., Van Dissen, R., McGuire, C.P., Hatem, A.E., Brown, N.D., and Langridge, R.M., 2018, Multimillennial incremental slip rate variability of the Clarence fault at the Tophouse Road site, Marlborough fault system, New Zealand: Geophysical Research Letters, v. 46, p. 717–725, https://doi.org/10.1029/2018GL080688.